PHYSICAL REVIEW E VOLUME 58, NUMBER 3 SEPTEMBER 1998

Model of hydrodynamic perturbation growth in the start-up phase of laser implosion

R. Ishizaki* and K. Nishihara
Institute of Laser Engineering, Osaka University, 2-6 Yamada-oka, Suita, Osaka 565-0871, Japan

(Received 10 July 1997; revised manuscript received 13 May 1998)

A simple analytical model is presented to study hydrodynamic perturbation growths driven by nonuniform laser ablation in the start-up phase in laser fusion. Propagation of a rippled shock and deformation of an ablation surface are studied for cases of initial target roughness and nonuniform laser irradiation. The study of the perturbation growth in the start-up phase is very important because it seeds the Rayleigh-Taylor instability in the subsequent acceleration and stagnation phases. Analytical solutions are obtained for temporal evolutions of the shock front ripple and the ablation surface deformation. As a result, it is seen that the shock front ripples oscillate and decay in both cases. On the other hand, there is an asymptotic amplitude of the ablation surface deformation in the case of uniform laser irradiation on a target with a rippled surface, and an asymptotic growth rate of the ablation surface ripple in the case of nonuniform laser irradiation on a smooth target. In both cases, it can be shown that a high intensity of laser irradiation causes the ablation surface to distort, and a short wavelength laser inhibits its deformation. Approximate formulas expressing the temporal behaviors of the shock front and the ablation surface are obtained in the weak shock limit. Those formulas are also applicable to a relatively strong shock. Analytical results agree quite well with recent experimental data for the shock front ripple and the areal mass density perturbation in the initial target roughness case. The behaviors of the shock front ripple and the ablation surface deformation are also investigated in the case where the nonuniformity of the laser irradiation oscillates with time. It can be seen that the deformation of the ablation surface is inhibited for a high oscillation frequency of the laser nonuniformity. [S1063-651X(98)06009-7]

PACS number(s): 52.35.Tc, 52.35.Py, 52.50.Jm

I. INTRODUCTION

To achieve ignition and high gain in inertial confinement fusion (ICF) [1,2], a spherical pellet must implode efficiently and symmetrically. A laser implosion process can be divided into three phases: start-up, acceleration, and stagnation phases. A shock wave driven by laser ablation propagates through a shell in the start-up phase, and shell acceleration then follows. The ablation surface and the interface between a hot core and surrounding cold main fuel are Rayleigh-Taylor (RT) unstable [3] in the acceleration and stagnation phases, respectively. Hydrodynamic perturbation growth in the start-up phase seeds the RT instability in the subsequent acceleration and stagnation phases. The study of the hydrodynamic perturbation growth in the shock compressed phase is thus essential for a better understanding of the RT instability, that is important not only in ICF but also in supernova explosions [4].

When ablation pressure is applied on a target with a rippled surface, a rippled shock wave is launched in accordance with the target surface. It is known that when a shock front is rippled, the phase of the ripple oscillates as the shock propagates. This is caused by lateral fluid motion behind the rippled shock front. Also, when a smooth target is nonuniformly irradiated by a laser beam, a rippled shock is driven by perturbed ablation pressure. The oscillation of the rippled shock generate hydrodynamic perturbations, and determine the initial conditions for the RT instability after shock breakout [5–8].

Hydrodynamic perturbations generated at the rippled shock front propagate through the shock compressed region, and induce deformation of the ablation surface. On the other hand, perturbed ablation pressure drives hydrodynamic perturbations in the shock compressed region, and affects the shock front ripple because the flow behind the shock is subsonic. The shock front ripple and the deformation of the ablation surface thus interact with each other through a sound wave and an entropy wave in the shock compressed region. It was shown in Ref. [9] that the temporal evolution of the rippled shock front and the deformation of the ablation surface are obtained by solving a linear wave equation in the shock compressed region with suitable boundary conditions that describe the ripple of the shock front and the deformation of the ablation surface. In this paper, a mathematical derivation of model equations is represented in detail, with their analytical solutions for various cases.

We consider a rippled shock driven by nonuniform laser ablation that is induced by an initial surface roughness of a target or by nonuniform laser irradiation on a smooth target. In the linear theory, the surface roughness and nonuniform irradiation are treated separately with different boundary conditions. As a result, analytical solutions of the model equation will be explicitly shown, and approximate formulas will be obtained in the weak shock limit. We show a good agreement between those formulas and the exact solutions not only for a weak shock but also for a relatively strong shock. Some of the solutions are compared with recent experimental results [5], and good agreements between them are obtained as shown in Ref. [9].

It should be mentioned that since the model is based on linear theory and the assumption of a stationary laser ablation as the zeroth order hydrodynamics, the theory may be difficult to apply directly to imprint experiments [10–14]. In

---

*Present address: National Institute for Fusion Science, 322-6 Oroshi-cho, Toki, Gitu 509-5292, Japan. Electronic address: ishizaki@nifs.ac.jp those experiments, a significant imprint may be created by nonuniform laser irradiation before the stationary laser ablation takes place. Despite this fact, analytical solutions are useful to understand the underlying physics and the dependence on target and laser parameters.

Our model uses the variable transformation introduced by Zaidel [15] to solve the linear wave equation in the shock compressed region with boundary conditions such as the Rankine-Hugoniot (RH) jump condition at the shock front [15–18] and the Chapman-Jouguet (CJ) deflagration jump condition at the laser ablation surface [19]. The RH jump condition gives relations of physical variables across the shock front, while the CJ deflagration jump condition relates physical variables at the ablation surface with those at the sonic point. It is thus assumed implicitly that a wavelength of target surface roughness or laser nonuniformity is very long compared with the width of the ablation layer. This assumption may be suitable for the case of laser irradiation with a weak intensity in which the width of the ablation layer is short, because the width is proportional to the mean free path determined by electron temperature at the sonic point [19]. If the wavelength of the perturbation is comparable to or shorter than the width, the thermal smoothing in the ablation layer should be taken into account. It should also be mentioned that we choose ''plausible'' boundary conditions at the sonic point because the flow expands supersonically in a region beyond the sonic point, and neither sound nor entropy waves in this region can cross the sonic point and affect the shock compressed region.

In spite of these assumptions, we can derive many significant features of the problems from the simple model. Initially, the amplitude of the shock surface ripple decays rapidly compared with that driven by a rippled rigid piston, because of the mass ablation across the ablation surface. The amplitude of the ablation surface ripple approaches a finite value in the case of the target surface roughness. It should be noted that the growth of the ablation surface ripple is different from the Richtmyer-Meshkov (RM) instability, because in the RM instability there is a finite growth rate and no asymptotic amplitude [17,20,21]. On the other hand, in the case of nonuniform laser irradiation the growth rate of the ablation surface ripple reaches an asymptotic value. Therefore, it may be meaningless to express an amount of laser imprint by an equivalent initial surface roughness [22], because the ablation surface ripple increases with time.

A weak intensity laser can be used as a prepulse in the start-up phase in order to prevent an entropy increase. However, a laser with a relatively strong intensity (for example, a ''picket fence'' pulse laser [23]) is also used in order to promote the ablative stabilization in the acceleration phase. It is thus important to investigate the laser intensity dependence of hydrodynamic perturbations. In addition, it is also interesting to estimate the laser wavelength dependence. As a result, it will be shown that laser irradiation at a high intensity causes the ablation surface to distort, and laser irradiation at a short wavelength inhibits its deformation.

A partially coherent light [24,25] can be used as a laser beam, so that the nonuniformity of the laser irradiation is smoothed out. In order to estimate target perturbations caused by the time varying nonuniformity of the laser irradiation, it may be important to study the case when the nonuniformity of the laser irradiation oscillates with time. The behavior of the shock front ripple and the ablation surface deformation is investigated in such a case. It can be seen that the deformation of the ablation surface is inhibited for a high oscillation frequency.

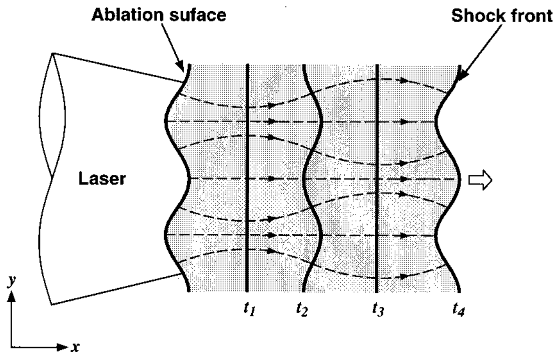

FIG. 1. Illustration of rippled shock propagation driven by nonuniform laser ablation induced by the initial surface roughness of a target. Solid and dashed lines show shock fronts at different times and rays, respectively. t_1, t_2, t_3, and t_4 correspond to times when the amplitude of the shock front ripple become zero, maximum (reversed), zero, and maximum, respectively ($t_1 < t_2 < t_3 < t_4$).

In Sec. II A, the zeroth order profile of a stationary shock wave driven by a steady laser ablation is examined. The profile is determined by applying the RH jump condition at the shock front and the CJ deflagration jump condition at the ablation surface. In Sec. II B, we describe an analysis for perturbed quantities. The perturbation analysis solves a wave equation for pressure perturbation in the shock compressed region. In Sec. II C, we explain the boundary conditions at the shock front and at the ablation surface to solve the wave equation. In Sec. III, we analyze the temporal evolution of the shock front ripple and the ablation surface deformation by using the pressure perturbation in the case when the laser is uniformly irradiated on a target with a rippled surface. In Sec. IV, we carry out an analysis similar to that in Sec. III in the case when the laser is nonuniformly irradiated on a smooth target. The cases of constant and oscillating laser irradiation with time are discussed in Secs. IV A and IV B, respectively. A summary is given in Sec. V.

II. ANALYTICAL MODEL

Laser ablation drives a shock wave forward. In the case when an initial surface roughness of a target is present, a rippled shock wave is launched in accordance with the target surface roughness. The rippled shock front oscillates as the shock propagates. Figure 1 shows a schematic of rippled shock fronts (solid lines) driven by nonuniform laser ablation induced by the initial surface roughness of a target at successive times of $t_1 < t_2 < t_3 < t_4$. From experience based on geometrical optics, we introduce ''rays'' defined as orthogonal trajectories of successive rippled shock fronts. The rays are shown as dashed lines. Initially, the shock driven by the ablation propagates normally to the ablation surface. One ray tube becomes narrower and another ray tube becomes broader as the shock propagates, and the difference of the ray tube widths reaches a maximum at the time $t = t_1$. At this time the density perturbation behind the shock front reaches

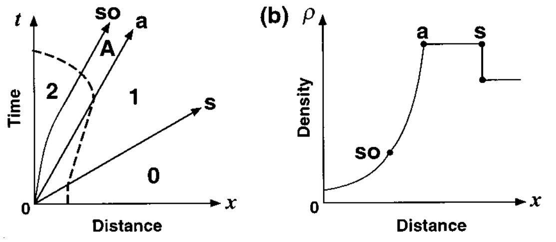

FIG. 2. Schematic diagram of shock propagation driven by laser ablation; (a) x-t diagram; (b) density profile at a certain time. s, a, and so denote the shock front, ablation front, and sonic point, respectively. 0, 1, A, and 2 denote the unperturbed region, shock compressed region, deflagration region, and isothermal rarefaction region, respectively. The dashed line in (a) shows fluid flow.

a maximum because the density is proportional to the inverse of the ray tube width. The transverse velocity perturbation is zero at $t=t_1$ because the tangent of the ray trajectory corresponds to the direction of the fluid velocity behind the shock front. Since the pressure reaches a maximum in the narrowest tube and a minimum in the broadest tube, the pressure perturbation has its maximum value at the time $t=t_1$. The pressure perturbation generates the transverse flow. Therefore, the phase of the fluid motion is reversed, and at the time $t=t_2$ the ray tube widths become the same (i.e., the density and pressure perturbations become zero) and the transverse velocity perturbation reaches its maximum value. These processes repeat at $t=t_3$ and $t=t_4$. The shock front ripple thus oscillates with the propagation. The rippled shock propagation results in a hydrodynamic perturbation behind the shock, and a deformation of the ablation surface.

In this section, we develop an analytical model in order to investigate a rippled shock wave and a nonuniform laser ablation caused by the initial surface roughness of a target or nonuniform laser irradiation on a smooth target. We will show that hydrodynamic perturbations caused by the rippled shock propagation can be obtained by solving a sound wave equation in the shock compressed region, with suitable boundary conditions at the shock front and the ablation surface.

A. Zeroth order profile

At first, we briefly sketch the zeroth order profile of a stationary shock wave driven by a steady laser ablation. The energy increase in the ablation layer due to electron thermal conduction is thought to be due to combustion in a chemical reaction wave, and thus the ablation layer is characterized by the deflagration wave. The ablation acts as a piston and drives a shock wave forward. Isothermal expansion follows the deflagration, since the flow is generally nonstationary behind the Chapman-Jouguet point where the flow velocity equals the local sound speed in a reference frame moving with the ablation surface. The domain can be then separated into four regions by the shock front, ablation front, and sonic point, as shown in Fig. 2. We label these regions 0, 1, A, and 2 from right to left. Region 0 is a uniform state ahead of the shock; region 1 is a shock compressed region; region A is an ablation layer between the ablation front and the sonic point; and region 2, beyond the sonic point, is an isothermal rarefaction region where the flow is self-similar and supersonic. The electron heat conduction should be taken into account to obtain the structure of the ablation layer. However, physical variables of the whole regions are simply obtained by means of the jump conditions at the shock front and through the ablation layer.

We can write the mass, momentum, and energy conservation equations across the shock front (between regions 0 and 1) as

$$\rho_0 u_s = \rho_1 (u_s - v_{x1}), \tag{2.1a}$$

$$p_0 + \rho_0 u_s^2 = p_1 + \rho_1 (u_s - v_{x1})^2, \tag{2.1b}$$

$$h_0 + \tfrac{1}{2} u_s^2 = h_1 + \tfrac{1}{2} (u_s - v_{x1})^2, \tag{2.1c}$$

and across the ablation layer (between regions 1 and 2) as

$$\rho_1 (u_a - v_{x1}) = \rho_2 (u_a - v_{x2}), \tag{2.2a}$$

$$p_1 + \rho_1 (u_a - v_{x1})^2 = p_2 + \rho_2 (u_a - v_{x2})^2, \tag{2.2b}$$

$$h_1 + \frac{1}{2}(u_a - v_{x1})^2 + \frac{I}{\rho_1 (u_a - v_{x1})} = h_2 + \frac{1}{2}(u_a - v_{x2})^2, \tag{2.2c}$$

where u_s, u_a, and v_x are the shock front, ablation surface velocities, and fluid velocity in a laboratory frame, and p, ρ, and h are the pressure, density, and enthalpy, respectively. I is the absorbed laser intensity. $\nu = (\gamma+1)/(\gamma-1)$, and γ is the isentropic exponent. The subscripts 0, 1, and 2 denote the values of the regions 0, 1, and the sonic point, respectively. We can express u_s and $u_s - v_{x1}$ by the pressure p and specific volume $V(=1/\rho)$ from Eqs. (2.1a) and (2.1b) as

$$\frac{u_s}{V_0} = \frac{u_s - v_{x1}}{V_1} = \sqrt{\frac{p_1 - p_0}{V_0 - V_1}}. \tag{2.3}$$

Substituting Eq. (2.3) into Eq. (2.1c), and using the enthalpy equation for an ideal fluid $h = \gamma p V/(\gamma - 1)$, we obtain

$$(\nu_0 V_0 - V_1) p_0 - (\nu_1 V_1 - V_0) p_1 = 0. \tag{2.4}$$

The relations given by Eqs. (2.3) and (2.4) are familiar as the RH jump conditions of a shock wave. In the same way, we obtain relations at the ablation surface from Eq. (2.2) (see Appendix A):

$$\frac{u_a - v_{x1}}{V_1} = \frac{u_a - v_{x2}}{V_2} = \sqrt{\frac{p_1 - p_2}{V_2 - V_1}} = \dot{m} = \rho_1 v_a, \tag{2.5}$$

$$(\nu_1 V_1 - V_2) p_1 - (\nu_2 V_2 - V_1) p_2 = -\frac{2I}{\dot{m}}, \tag{2.6}$$

where $\dot{m}$ is the mass ablation rate, and v_a is the fluid velocity across the ablation surface, namely, the ablation velocity. The fluid velocity at the sonic point relative to the ablation surface is equal to the isothermal sound speed at the sonic point:

$$u_a - v_{x2} = \sqrt{p_2 V_2}. \tag{2.7}$$

These relations are referred to as the CJ deflagration jump conditions [19].

It is known that once the uniform state ahead of the shock and the absorbed laser intensity are given, one can uniquely determine the zeroth order variables in each region by using the jump conditions and the energy conservation of the whole system [19]. It is also possible to determine all zeroth order variables by using the jump conditions and specifying one of the variables, such as the ablation pressure, the mass ablation rate, or the density at the sonic point. In this paper we simply assume that the density at the sonic point is the laser cutoff density [26]. The sonic point density may not always be the cutoff density, especially for a short wavelength laser. However, this assumption is not so inaccurate in the case when a low-Z target (e.g., CH) is irradiated by a 0.53-μm laser. For a shorter wavelength laser, we can solve the zeroth order jump conditions by using the observed ablation pressure (p_1) or mass ablation rate ($\dot{m}$) instead of the cutoff density.

p_1 is approximately proportional to $I^{2/3}$ when the density at the sonic point is the laser cutoff density (see Appendix A). The analytical model described in this paper is applicable even to different ablation models [27] in which the laser intensity dependence of the ablation pressure $p_1(I)$ is not $I^{2/3}$, as will be discussed in Sec. IV A.

B. Perturbation analysis in shock compressed region

An initial surface roughness of a target or nonuniform laser irradiation on a smooth target induces perturbations of pressure, volume, and velocity in regions 1, A, and 2. We study the problem in a system of reference that moves with the shock compressed region, in which the coordinates are defined by $x'=x-v_{x1}t$ and $t'=t$. In this system, the shock front and the ablation surface moves with velocities, u_s-v_{x1} and $u_a-v_{x1}(=v_a)$, respectively. All perturbed quantities are assumed to depend on the transverse coordinate proportional to exp(iky), with a wave number k. We assume that the initial surface modulation of the target is given as $a_0\exp(iky)$ in the initial target roughness case, and the absorbed laser nonuniformity as $\delta I\exp(iky)$ in the nonuniform laser irradiation case, where a_0 and δI are the amplitude of a surface roughness and the nonuniformity of the absorbed laser intensity, respectively. Moreover, we assume a small perturbation $a_0 \ll \lambda (=2\pi/k)$ or $\delta I \ll I$, so that the equations can be linearized.

We can write the linearized fluid equations applied to the region 1 as

$$\frac{\partial}{\partial t'}\delta V_1 - V_1\left(\frac{\partial}{\partial x'}\delta v_{x1} + ik\delta v_{y1}\right) = 0, \tag{2.8a}$$

$$\frac{\partial}{\partial t'}\delta v_{x1} = -V_1\frac{\partial}{\partial x'}\delta p_1, \tag{2.8b}$$

$$\frac{\partial}{\partial t'}\delta v_{y1} = -ikV_1\delta p_1, \tag{2.8c}$$

$$\frac{\partial}{\partial t'}\delta s_1 = 0, \tag{2.8d}$$

where δp_1, δV_1, and δs_1 are the perturbations of the pressure, specific volume, and entropy in the compression region, respectively. δv_{x1} and δv_{y1} are x and y components of the perturbed fluid velocity, respectively. The perturbations δp_1, δV_1, and δs_1 are related through the law of thermodynamics and the equation of state for an ideal gas as

$$\frac{\delta s_1}{c_{v1}} = \frac{\delta p_1}{p_1} + \gamma_1\frac{\delta V_1}{V_1}, \tag{2.9}$$

where c_{v1} is the specific heat at constant volume in the region 1. From Eq. (2.8d), we see that the entropy perturbation is only a function of position x'. By using Eqs. (2.8) and (2.9), we obtain the homogeneous wave equation for the perturbed pressure:

$$\frac{\partial^2}{\partial t'^2}\delta p_1 = c_1^2\frac{\partial^2}{\partial x'^2}\delta p_1 - c_1^2k^2\delta p_1, \tag{2.10}$$

where c_1 is the sound speed in the region 1: $c_1=\sqrt{\gamma_1 p_1 V_1}$. Introducing new nondimensional independent variables r and θ defined by

$$r\cosh\theta = kc_1t' \equiv \hat{t}, \tag{2.11a}$$

$$r\sinh\theta = kx' \equiv \hat{x}, \tag{2.11b}$$

the general solution of Eq. (2.10) is written as [15,16,20]

$$\hat{p}_1 \equiv \frac{\delta p_1}{p_1} = \sum_\mu (D_\mu^a e^{+\mu\theta} + D_\mu^b e^{-\mu\theta})[D_\mu^c J_\mu(r) + D_\mu^d N_\mu(r)], \tag{2.12}$$

where J_μ and N_μ are Bessel and Neumann functions of the order μ, respectively. The coefficients D_μ^a, D_μ^b, D_μ^c, and D_μ^d, as well as the separation constant μ, must be determined by the initial and boundary conditions. The coordinates of both shock and ablation fronts with the new variables are defined as r_s, θ_s and r_a, θ_a, respectively. The domain of the variables are thus $r \geqslant 0$ and $\theta_a \leqslant \theta \leqslant \theta_s$.

C. Boundary conditions

We consider the boundary conditions at the shock front and the ablation surface. Let us introduce the amplitude of the shock front ripple as a_s. The total derivative of the amplitude with respect to time is then equal to the perturbation of the shock velocity, i.e., $\dot{a}_s \equiv da_s/dt' = \delta u_s$. We normalize the amplitude by the wave number $\hat{a}_s = ka_s$. By linearizing Eqs. (2.3) and (2.4), and with the assumption of no perturbation ahead of the shock, we obtain the relations among the perturbed quantities at the shock front:

$$\frac{\delta u_s}{c_1} = \frac{\dot{a}_s}{c_1} = \frac{d\hat{a}_s}{d\hat{t}} = \frac{1}{\cosh\theta_s}\frac{d\hat{a}_s}{dr_s} = K_1\hat{p}_1(r_s,\theta_s), \tag{2.13a}$$

$$\hat{v}_{x1}(r_s,\theta_s)=K_2\hat{p}_1(r_s,\theta_s), \tag{2.13b}$$

$$\hat{V}_1(r_s,\theta_s)=K_3\hat{p}_1(r_s,\theta_s), \tag{2.13c}$$

$$\hat{v}_{y1}(r_s,\theta_s)=K_4\hat{a}_s(r_s), \tag{2.13d}$$

where $\hat{V}_1=\delta V_1/V_1$, $\hat{v}_{x1}=\delta v_{x1}/c_1$, and $\hat{v}_{y1}=i\delta v_{y1}/c_1$, and the coefficients are defined as

$$K_1=\frac{\gamma_1+1}{4\gamma_1}\frac{1}{\beta_s},\quad K_2=\frac{M_s^2+1}{2\gamma_1 M_s^2}\frac{1}{\beta_s},$$

$$K_3=-\frac{1}{\gamma_1 M_s^2\beta_s^2},\quad K_4=\frac{v_{x1}}{c_1}=\frac{2(M_s^2-1)}{2\gamma_1 M_s^2-(\gamma_1-1)}\frac{1}{\beta_s}.$$

M_s and β_s are the shock Mach numbers for the fluids ahead of and behind the shock front, respectively. That is,

$$M_s=u_s/c_0$$

and

$$\begin{aligned}\beta_s&=(u_s-v_{x1})/c_1\\&=\sqrt{\{(\gamma_1-1)M_s^2+2\}/\{2\gamma_1 M_s^2-(\gamma_1-1)\}}.\end{aligned}$$

Substituting Eqs. (2.13b) and (2.13d) into Eqs. (2.8a) and (2.8b) at the shock front ($r=r_s$ and $\theta=\theta_s$), we obtain another shock boundary condition:

$$K_2\left[\frac{\partial\hat{p}_1}{\partial r}\right]_{r=r_s}+\frac{1}{\gamma_1 r_s}\left[\frac{\partial\hat{p}_1}{\partial\theta}\right]_{\theta=\theta_s}+K_4(\sinh\,\theta_s)\hat{a}_s(r_s)=0. \tag{2.14}$$

We use Eqs. (2.13a) and (2.14) as the boundary conditions in order to determine the coefficients in the general solution of $\hat{p}_1$ given by Eq. (2.12). Because the solution containing the Neumann function has been dropped in order to satisfy the initial condition $p_1(0,\theta)=$finite, we can rewrite Eq. (2.12) as

$$\hat{p}_1(r,\theta)=\sum_\mu\,(E_\mu e^{-\mu(\theta_s-\theta)}+F_\mu e^{-\mu(\theta-\theta_a)})J_\mu(r), \tag{2.15}$$

where $E_\mu=D_\mu^a D_\mu^c e^{\mu\theta_s}$ and $F_\mu=D_\mu^b D_\mu^c e^{-\mu\theta_a}$ are used in order to defend exponential terms of Eq. (2.12) against numerical divergence. Following Zaidel [15], let us define

$$A(s)=\int_0^\infty\hat{a}_s(r)e^{-sr}dr, \tag{2.16a}$$

$$P(s,\theta)=\int_0^\infty\hat{p}_1(r,\theta)e^{-sr}dr. \tag{2.16b}$$

Using the fact that the Laplace transform of $J_\mu(r)$ is $e^{-\mu q}/\cosh q$ by defining $s=\sinh q$, Eq. (2.15) becomes

$$P(s,\theta)=\sum_\mu\,(E_\mu e^{-\mu(\theta_s-\theta)}+F_\mu e^{-\mu(\theta-\theta_a)})\frac{e^{-\mu q}}{\cosh q}. \tag{2.17}$$

Using Eq. (2.17) and the fact that the Laplace transform of $\mu J_\mu(r)/r$ is $e^{-\mu q}$, we can write Eqs. (2.13a) and (2.14) as

$$A(s)=\frac{K_1(\cosh\,\theta_s)P(s,\theta_s)+\hat{a}_0}{\sinh q}, \tag{2.18a}$$

$$\begin{aligned}&K_2P(s,\theta_s)\sinh q-K_2\hat{p}_{10}+\sum_\mu\frac{1}{\gamma_1}(E_\mu-F_\mu e^{-\mu(\theta_s-\theta_a)})\\&\quad\times e^{-\mu q}+K_4(\sinh\,\theta_s)A(s)=0,\end{aligned} \tag{2.18b}$$

where $\hat{a}_0$ and $\hat{p}_{10}$ are initial values of the normalized shock ripple amplitude and the normalized pressure perturbation at the shock front, respectively. That is, $\hat{a}_0=ka_0$ and $\hat{p}_{10}=\hat{p}_1(0,\theta_s)$. Substituting Eq. (2.18a) into Eq. (2.18b), we obtain

$$\begin{aligned}&\sum_m\,(K_2\,\sinh^2 q+K_1K_4\,\sinh\,\theta_s\,\cosh\,\theta_s)(E_m+F_m e^{-m(\theta_s-\theta_a)})e^{-mq}+\sum_m\frac{1}{\gamma_1}\sinh q\,\cosh q(E_m-F_m e^{-m(\theta_s-\theta_a)})e^{-mq}\\&\quad-K_2\hat{p}_{10}\sinh q\,\cosh q+K_4\hat{a}_0\,\sinh\,\theta_s\,\cosh q=0.\end{aligned} \tag{2.19}$$

E_m and F_m are determined by the independent equations obtained by setting the coefficients of e^{-mq} equal to zero for all m. The index μ in Eq. (2.18) is replaced by a positive integer m, so that terms with $\hat{a}_0$ and $\hat{p}_{10}$ are consistent with the other terms in Eq. (2.19).

To close the problem we consider the boundary conditions at the ablation surface. In our analysis, we regard the linearized CJ deflagration jump conditions as the boundary conditions at the ablation surface by assuming that the width of the ablation layer A in Fig. 2 is very short compared with the wavelength of the perturbation, $\lambda(=2\pi/k)$. For the perturbation of which wavelength is comparable to the width of the ablation layer or shorter than the width, one should consider the thermal smoothing effect in the ablation layer.

In the same way as the shock front ripple, we introduce the amplitude of the ablation surface ripple as a_a. The total time derivative of the amplitude is equal to the perturbation of the ablation surface velocity, i.e., $\dot{a}_a\equiv da_a/dt'=\delta u_a$. After the linearization of the CJ deflagration jump conditions with complicated calculation as shown in Appendix B, we obtain

$$\frac{\dot{a}_a - \delta v_{x1}}{v_a} = \frac{\hat{p}_1 - \hat{p}_2 + \hat{V}_1 - \bar{M}\hat{V}_2}{1-\bar{M}}, \tag{2.20a}$$

$$\frac{\dot{a}_a - \delta v_{x2}}{c_2} = \frac{1}{1-\bar{M}}\left(\hat{p}_1 - \hat{p}_2 + \bar{M}\hat{V}_1 + \frac{\bar{M}(1-3\bar{M})}{1+\bar{M}}\hat{V}_2\right), \tag{2.20b}$$

$$L_1\hat{p}_1 + L_2\hat{V}_1 + L_3\hat{p}_2 + L_4\hat{V}_2 = L_5\hat{I}. \tag{2.20c}$$

In the above equations, the coefficients are

$$L_1 = \frac{1+\bar{M}}{\bar{M}} - \nu_1\frac{2-\bar{M}}{1-\bar{M}} + \nu_2\frac{(1+\bar{M})^2}{4\bar{M}(1-\bar{M})},$$

$$L_2 = -\nu_1\frac{1}{1-\bar{M}} + \nu_2\frac{(1+\bar{M})^2}{4(1-\bar{M})},$$

$$L_3 = -\frac{1+3\bar{M}}{2\bar{M}} + \nu_1\frac{1}{1-\bar{M}} + \nu_2\frac{(1+\bar{M})(1-3\bar{M})}{4\bar{M}(1-\bar{M})},$$

$$L_4 = \frac{1-\bar{M}}{2} + \nu_1\frac{\bar{M}}{1-\bar{M}} + \nu_2\frac{(1+\bar{M})(1-3\bar{M})}{4(1-\bar{M})},$$

$$L_5 = \frac{1-\bar{M}^2}{2\bar{M}} - \nu_1 + \nu_2\frac{(1+\bar{M})^2}{4\bar{M}},$$

where $\hat{I} = \delta I/I$ and $\bar{M} = \gamma_1(v_a/c_1)^2$. v_a/c_1 represents the ablation Mach number which is much smaller than unity in general. We define $\hat{p}_2 = \delta p_2/p_1$, $\hat{V}_2 = \delta V_2/V_1$, and $\hat{v}_{x2} = \delta v_{x2}/c_1$, where δp_2, δV_2, and δv_{x2} are the perturbations of the pressure, specific volume, and fluid velocity at the sonic point. Equation (2.20) gives relations between the perturbations at the ablation front and those at the sonic point.

We assume that the first-order quantities at the sonic point satisfy the condition that the local Mach number is equal to unity [28]:

$$\frac{\dot{a}_a - \delta v_{x2}}{c_2} = \frac{1}{2}\left(\frac{\delta p_2}{p_2} + \frac{\delta V_2}{V_2}\right) = \frac{\hat{p}_2 + \bar{M}\hat{V}_2}{1+\bar{M}}. \tag{2.21}$$

In addition, we assume

$$\hat{V}_2 = 0, \tag{2.22}$$

because the density of the sonic point is taken to be the laser cutoff density [26]. It is noted that we are not solving the perturbation in region 2. Rather, we replace that physics with Eq. (2.21), and replace the assumption with Eq. (2.22). In this way, Eqs. (2.19)–(2.22) give enough boundary conditions for $\hat{p}_1$ to be solved. This can be done because the flow in region 2 expands supersonically, and neither sound nor entropy waves in region 2 can cross the sonic point and affect the flow in region 1. The assumption of $\delta V_2 = 0$ may not be a unique boundary condition. As a matter of fact, we obtain similar results, as will be explained in Sec. III, even if we choose the boundary condition $\delta T_2 = 0$ (T is the temperature). The boundary condition $\delta T_2 = 0$ corresponds to the assumption that large electron thermal conduction smooth out the temperature perturbation near the sonic point because of high temperature. As discussed in detail in Appendix C, both boundary conditions of $\delta V_2 = 0$ and $\delta T_2 = 0$ result in a similar relation between the pressure and density perturbations at the ablation surface. That is, the perturbation of the ablation pressure is very small compared with that of the density at the ablation surface. This feature of the ablation is also found in simulations [29] without these assumptions. Therefore, it should be possible to solve the problem in region 1 by choosing ''plausible'' boundary conditions at the sonic point.

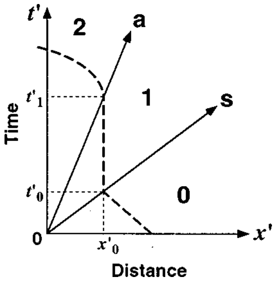

FIG. 3. x-t diagram of shock propagation driven by laser ablation in a system of reference that moves with the shock compressed region. s, a, 0, 1, A, and 2 are the same as in Fig. 2. Dashed line shows fluid flow. x_0' is an arbitrary coordinate in the compression region, and t_0' and t_1' are times when the fluid at x_0' crosses the shock front and the ablation surface, respectively.

Eliminating $\hat{p}_2$, $\hat{V}_2$, and $\dot{a}_a - \delta v_{x2}$ by using Eqs. (2.20b), (2.20c), (2.21), and (2.22), we obtain a relation among $\hat{p}_1$, $\hat{V}_1$, and $\hat{I}$:

$$\hat{p}_1 = L_6\hat{V}_1 + \frac{2}{3}\hat{I}, \tag{2.23}$$

where

$$L_6 = \frac{1}{L_5}\left[\frac{(\bar{M}+1)(3\bar{M}+1)}{6} + \nu_1\frac{\bar{M}+2}{3} - \nu_2\frac{(\bar{M}+1)^2}{4}\right].$$

At last, we consider the entropy perturbation in region 1. Figure 3 shows an x-t diagram in a system of reference that moves with the shock compressed region. The entropy perturbation is conserved along a flow line as shown by Eq. (2.8d). Then

$$\hat{s}_1(x_0', t_0') = \hat{s}_1(x_0', t_1'), \tag{2.24}$$

where $\hat{s}_1 = \delta s_1/c_{v1}$, and t_0', t_1', and x_0' are defined in Fig. 3. x_0' is an arbitrary coordinate in the compression region, and t_0' and t_1' are times when the fluid at x_0' crosses the shock front and the ablation surface, respectively. Using Eq. (2.9) and the fact that Eqs. (2.13c) and (2.23) represent the relations between $\hat{p}_1$ and $\hat{V}_1$ at the shock front and ablation surface, respectively, we can write Eq. (2.24) as

$$\hat{p}_1(x_0',t_1')=L_7\hat{p}_1(x_0',t_0')+L_8\hat{I}(t_1'), \tag{2.25}$$

where the coefficients are

$$L_7=\frac{L_6(1-K_3)}{L_6+\gamma_1},\quad L_8=\frac{2\gamma_1}{3(L_6+\gamma_1)}.$$

Transforming Eq. (2.25) from the system of x' and t' to the system of r and θ, we have

$$\hat{p}_1(r_a,\theta_a)=L_7\hat{p}_1(\alpha r_a,\theta_s)+L_8\hat{I}(r_a), \tag{2.26}$$

where $\alpha=\sinh\theta_a/\sinh\theta_s$. Substituting Eq. (2.15) into Eq. (2.26) and expanding the Bessel function with respect to r_a, we obtain

$$\sum_{m=0}^{\infty}\sum_{l=0}^{\infty}[(E_m e^{-m(\theta_s-\theta_a)}+F_m)-L_7\alpha^{m+2l}\times(E_m+F_m e^{-m(\theta_s-\theta_a)})]\frac{(-1)^l}{l!(m+l)!}\left(\frac{r_a}{2}\right)^{m+2l}=L_8\hat{I}(r_a). \tag{2.27}$$

The expansion of $\hat{I}$ with respect to r_a is written as

$$\hat{I}(r_a)=\sum_{n=0}^{\infty}\frac{1}{n!}\left[\frac{d^n\hat{I}}{dr^n}\right]_{r=0}r_a^n=\sum_{n=0}^{\infty}\phi_n r_a^n, \tag{2.28}$$

where $\phi_n=[d^n\hat{I}/dr^n]_{r=0}/n!$. E_m and F_m are determined from the independent equations given by setting the coefficients of r_a^n equal to zero for all n after substituting Eq. (2.28) into Eq. (2.27). We have found that E_m and F_m with even m are independent of E_m and F_m with odd m in Eq. (2.27) as well as in Eq. (2.19). We can obtain the local pressure perturbation in the shock compressed region by using the solution given by Eq. (2.15) after the coefficients have been determined from Eqs. (2.19) and (2.27), and can calculate all other perturbed variables.

III. HYDRODYNAMIC PERTURBATION DRIVEN BY AN INITIAL SURFACE ROUGHNESS OF A TARGET

We consider a rippled shock wave driven by an initial corrugated surface. Since the rippled shock wave is launched in accordance with the target surface, initial conditions are given by

$$\hat{a}_s(0)=\hat{a}_a(0)=\hat{a}_0,\quad \hat{I}(r_a)=0\quad(\phi_m=0), \tag{3.1}$$

and there is no initial perturbation of the pressure:

$$\hat{p}_1(0,\theta)=\hat{p}_{10}=0\quad(\theta_a\leqslant\theta\leqslant\theta_s). \tag{3.2}$$

The separation constant must be a positive odd integer to satisfy both the initial conditions (3.1) and (3.2) and the boundary conditions (2.19) and (2.27). Equation (2.15) thus becomes

$$\hat{p}_1(r,\theta)=\sum_{n=0}^{\infty}(E_{2n+1}e^{-(2n+1)(\theta_s-\theta)}+F_{2n+1}e^{-(2n+1)(\theta-\theta_a)})J_{2n+1}(r). \tag{3.3}$$

Substituting Eq. (3.3) into Eq. (2.13a) and integrating with respect to r_s with the initial condition Eq. (3.1), we can write the shock front ripple a_s as

$$\hat{a}_s(r_s)=\hat{a}_0+K_1(\cosh\theta_s)\sum_{n=0}^{\infty}(E_{2n+1}+F_{2n+1}e_{2n+1})\times\int_0^{r_s}J_{2n+1}(r)dr, \tag{3.4}$$

where $e_n=e^{-n(\theta_s-\theta_a)}$. Note also the relation which is obtained from Eq. (2.19) when $q=0$:

$$\sum_{n=0}^{\infty}(E_{2n+1}+F_{2n+1}e_{2n+1})=-\frac{\hat{a}_0}{K_1\cosh\theta_s}. \tag{3.5}$$

It can be seen from Eqs. (3.4) and (3.5) that $\hat{a}_s(r_s)\rightarrow 0$ when $r_s\rightarrow\infty$. Equation (3.4) can be expressed in a form

$$\hat{a}_s(r_s)=\sum_{n=0}^{\infty}G_{2n}J_{2n}(r_s), \tag{3.6}$$

where the coefficients G are

$$G_0=\hat{a}_0,$$

$$G_{2n}=2\hat{a}_0+2K_1(\cosh\theta_s)\sum_{k=0}^{n-1}(E_{2k+1}+F_{2k+1}e_{2k+1}). \tag{3.7}$$

The perturbed density in the compression region is not given by the isentropic formula because of the entropy perturbation generated at the shock front. The local density perturbation is given by Eq. (2.9) if the entropy perturbation is obtained. Since the entropy perturbation is constant along a flow line as shown by Eq. (2.8d), we can regard that the entropy perturbation induced at the rippled shock front propagates with the fluid. The specific volume perturbation is thus written as

$$\hat{V}_1(r,\theta)=-\frac{1}{\gamma_1}\hat{p}_1(r,\theta)+\left(K_3+\frac{1}{\gamma_1}\right)\hat{p}_1\left(r\frac{\sinh\theta}{\sinh\theta_s},\theta_s\right). \tag{3.8}$$

We can obtain the x component of the velocity perturbation by solving Eq. (2.8b) with Eq. (2.13b) (refer to Appendix D):

$$\hat{v}_{x1}=\sum_{n=0}^{\infty}(Q_{2n+1}e^{-(2n+1)(\theta_s-\theta)}+R_{2n+1}e^{-(2n+1)(\theta-\theta_a)})\times J_{2n+1}(r)+\sum_{n=0}^{\infty}S_{2n+1}J_{2n+1}\left(r\frac{\sinh\theta}{\sinh\theta_s}\right), \tag{3.9}$$

where the coefficients Q, R, and S are given by

$$Q_{2n+1}=-\frac{1}{\gamma_1}\left(2\sum_{k=0}^{n} E_{2k+1}e^{2(n-k)\theta_s}-E_{2n+1}\right), \tag{3.10a}$$

$$R_{2n+1}=\frac{1}{\gamma_1}\left(2\sum_{k=0}^{n} F_{2k+1}e^{-2(n-k)\theta_a}-F_{2n+1}\right), \tag{3.10b}$$

$$S_{2n+1}=K_2(E_{2n+1}+F_{2n+1}e_{2n+1})-(Q_{2n+1}+R_{2n+1}e_{2n+1}). \tag{3.10c}$$

In the same way, we can also obtain the y component of the velocity perturbation by solving Eq. (2.8c) with Eq. (2.13d) (refer to Appendix D).

Let us consider the ablation surface deformation a_a. Using Eqs. (2.20a), (2.20c), (2.22), and (2.23), $\dot{a}_a$ is given by

$$\begin{aligned}\frac{\dot{a}_a}{c_1}=\frac{d\hat{a}_a}{d\hat{t}}=\frac{1}{\cosh\,\theta_a}\frac{d\hat{a}_a}{dr_a}&=\hat{v}_{x1}+L_9\hat{p}_1+L_{10}\hat{I}\\ &=\sum_{n=0}^{\infty} X_{2n+1}J_{2n+1}(r_a)+L_{10}\hat{I},\end{aligned} \tag{3.11}$$

where the coefficients are defined as

$$L_9=\frac{v_a}{2c_1}\left(1+\frac{\overline{M}+2}{L_6}\right),\quad L_{10}=-\frac{v_a}{c_1}\frac{\overline{M}+2}{3L_6},$$

and

$$\begin{aligned}X_1&=W_1+S_1\alpha,\\ X_{2n+1}&=W_{2n+1}+S_{2n+1}\alpha^{2n+1}\\ &\quad+\sum_{k=0}^{n-1}(W_{2k+1}+S_{2k+1}\alpha^{2n+1}-X_{2k+1})\\ &\quad\times\frac{(-1)^{n-k}(2n+1)!}{(n-k)!(n+k+1)!},\end{aligned} \tag{3.12}$$

with

$$W_{2n+1}=(Q_{2n+1}+L_9E_{2n+1})e_{2n+1}+(R_{2n+1}+L_9F_{2n+1}), \tag{3.13}$$

where we used Eqs. (3.3) and (3.9) in order to determine the coefficient X. Integrating Eq. (3.11) with respect to r_a with the initial condition Eq. (3.1), we obtain

$$\hat{a}_a(r_a)=\hat{a}_0+2\,\cosh\,\theta_a\sum_{n=1}^{\infty}\left[\left(\sum_{k=0}^{n-1}X_{2k+1}\right)J_{2n}(r_a)\right]. \tag{3.14}$$

$\hat{a}_a$ is a function of $r_a=kc_1t\sqrt{1-\{(u_a-v_{x1})/c_1\}^2}$ because the ablation surface propagates along the trajectories of $x'=(u_a-v_{x1})t'$.

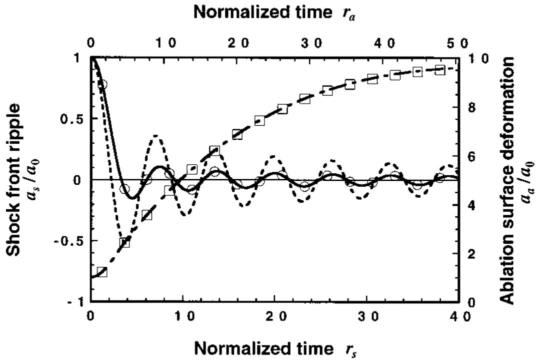

FIG. 4. Normalized amplitude of the shock front ripple a_s/a_0 as a function of normalized time, r_s; and the normalized amplitude of the ablation surface deformation a_a/a_0 as a function of normalized time, r_a. Solid and dot-dashed lines show a_s/a_0 and a_a/a_0, respectively. Circles and squares show the shock front ripple and ablation surface deformation, respectively, when $\delta T_2=0$ instead of $\delta V_2=0$. The dotted line shows a_s/a_0 driven by a rippled piston.

Figure 4 shows the normalized perturbation amplitude of the rippled shock front (solid line) a_s/a_0 as a function of the normalized time, r_s, and that of the ablation front (dot-dashed line) a_a/a_0 as a function of the normalized time, r_a. The parameters used are a laser intensity of $I=4\times10^{13}$ W/cm^2, a laser wavelength of $\lambda_L=0.53$ μm, a mass density of $\rho_0=1.06$ g/cm^3 (CH target), a pressure of $p_0=0.703$ Mbar (equivalent to $T_0=1$ eV), and isentropic exponents of $\gamma_0=3$, $\gamma_1=3$, and $\gamma_2=\frac{5}{3}$. Once a rippled shock is launched, a pressure perturbation is induced by the lateral fluid motion behind the shock front. The pressure perturbation causes the ripple of the shock front to be reversed and subsequently to oscillate, while the pressure perturbation increases the deformation of the ablation front monotonously. The amplitude of the shock ripple decays as the shock propagates. Since the pressure perturbation at the ablation surface also decays with time, the deformation of the ablation surface approaches a finite value as shown in Fig. 4. It takes a longer time for an ablation surface deformation to reach an asymptotic value as compared with an oscillation period of a rippled shock. It should also be noted that the increase of the ablation surface deformation is different from the RM instability, because in the RM instability there is a finite growth rate, $\dot{a}_a\neq0$ and thus no asymptotic amplitude [17,20,21]. Circles and squares show the shock front ripple and the ablation surface deformation, respectively, for the case when we choose $\delta T_2=0$ instead of $\delta V_2=0$ as the boundary condition at the sonic point. They coincide with the results of $\delta V_2=0$.

We compare a rippled shock wave driven by laser ablation with that driven by a rippled rigid piston (dotted line) [16,18] in Fig. 4. As clearly seen in Fig. 4, the amplitude of the shock surface ripple driven by the ablation decays rapidly compared with that driven by the rigid piston. That difference can be understood from Fig. 5. Figures 5(a) and 5(b) illustrate rippled shock fronts (s) and ablation surfaces (a) immediately after the shock is driven and later, respectively. The lateral fluid motion behind the rippled shock front is shown by arrows in Fig. 5(a). The fluid centered by the lateral motion flows out to both the shock and ablation fronts, as shown by arrows in Fig. 5(b). The fluid motion to the shock front causes the shock front ripple to decrease, and the phase of the ripple to be subsequently reversed. On the other hand, the fluid motion to the ablation front causes the ablation surface deformation to grow. Moreover, there is mass flow across the ablation surface that promotes fluid motion to

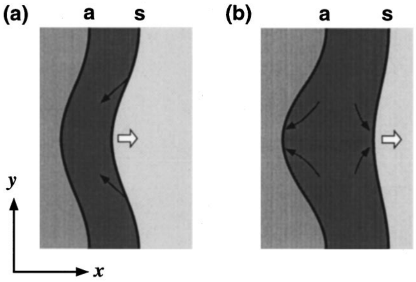

FIG. 5. Illustrations of rippled shock front and ablation surface (a) immediately after the shock is driven by uniform laser irradiation on a target with a rippled surface. (b) A little later. s and a are the same as in Fig. 2. Black arrows show the fluid flow, and white arrows show the direction of shock propagation.

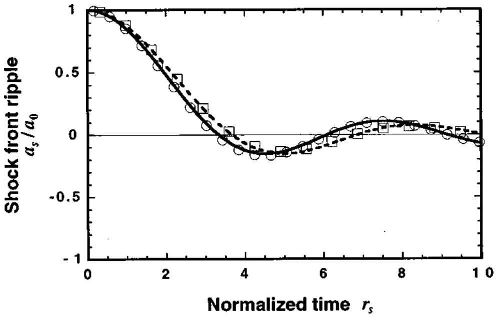

FIG. 6. Normalized amplitude of the shock front ripple a_s/a_0 as a function of normalized time, r_s. Dotted and solid lines show exact solutions of a_s/a_0 for absorbed laser intensities of $I=1\times10^{12}$ and 4×10^{13} W/cm^2, respectively. Squares and circles are corresponding approximate formulas.

the ablation surface. In the case of the rippled piston, there is neither piston surface deformation nor mass flow across the surface. Therefore, in the case of the ablation, the pressure perturbation behind the shock decays faster and the shock front ripple also decays rapidly compared with the case of the rigid piston. However, it should be noted that in both cases the amplitude of the rippled shock surface decays asymptotically in proportion to the reciprocal of the square root of time, $t^{-1/2}$.

In a weak shock limit, in the expression of a_s given by Eqs. (3.6) and (3.7), the first and second terms including E_1 and F_1 are dominant. Using the fact of $L_7\propto L_6\propto 1/L_5\propto\overline{M}\propto(v_a/c_1)^2\ll1$, from Eqs. (2.19) and (2.27) E_1 and F_1 are written as

$$E_1\simeq-\frac{2\gamma_1K_4\hat{a}_0\sinh\theta_s}{(\gamma_1K_2+1)-(\gamma_1K_2-1)e_1^2}, \tag{3.15a}$$

$$F_1\simeq\frac{2\gamma_1K_4\hat{a}_0\sinh\theta_s e_1}{(\gamma_1K_2+1)-(\gamma_1K_2-1)e_1^2}. \tag{3.15b}$$

In addition, using $\theta_a\ll1$ (equivalent to $v_a/c_1\ll1$), we obtain

$$\frac{a_s(t)}{a_0}\simeq J_0(r_s)+\frac{2M_s^2+2}{3M_s^2+1}J_2(r_s) \times\left[r_s=kc_1t\sqrt{1-(u_s-v_{x1})^2/c_1^2}\right]. \tag{3.16}$$

We show the comparison between this approximate formula (symbols) and the exact solution (lines) in Fig. 6. Squares and the dotted line and circles and the solid line represent the shock front behaviors with $I=1\times10^{12}$ W/cm^2 ($M_s=1.15$) and $I=4\times10^{13}$ W/cm^2 ($M_s=3.43$), respectively. The formula given by Eq. (3.16) agrees quite well with the exact solution not only for a small Mach number, but also for a relatively large Mach number. The shock front ripple is reversed faster for a larger shock Mach number, as shown in Fig. 6. Since the lateral flow behind the rippled shock front is larger in the case of the stronger shock, the flow causes the shock front ripple to decrease faster (see Fig. 5). The shock front ripple thus decreases and is reversed more quickly. In the weak shock limit, the surface ripple of the shock wave driven by a rippled piston is approximately given by [15]

$$\frac{a_s(r_s)}{a_0}\simeq J_0(r_s)+2\frac{(2\beta_s^2-1)M_s^2+1}{(2\beta_s^2+1)M_s^2+1}J_2(r_s) +2\left[1-\frac{4M_s^2}{(2\beta_s^2+1)M_s^2+1}\times\frac{(\beta_s^2M_s^2+2)(1+3\beta_s^2)+M_s^2\beta_s^2(3+\beta_s^2)}{(M_s^2+1)(1+3\beta_s^2)+2M_s^2\beta_s^2(3+\beta_s^2)}\right]J_4(r_s). \tag{3.17}$$

It should be noted that shocks driven by both ablation and piston have the same behavior for a very weak shock $M_s\simeq1$ (equivalent to $\beta_s\simeq1$), as shown by Eqs. (3.16) and (3.17). Since in that limit the shocks propagate approximately with a sound speed in a reference system that moves with the shock compressed region, the information of the ablation surface deformation and mass flow across the ablation surface can no longer reach the shock front. Therefore, the shock front ripples behave the same way for both cases in the weak shock limit.

On the other hand, the calculation of a_a is not as straightforward as that of a_s. It seems reasonable that in the weak shock limit the coefficient X expressed by Eq. (3.12) is approximated as

$$X_{2n+1}\simeq X_3e^{-2(n-1)\theta_a}\quad(n\geq1). \tag{3.18}$$

Therefore, substituting Eq. (3.18) into Eq. (3.14), we can write a_a as

$$\hat{a}_a(r_a)\simeq\hat{a}_0+X_1[1-J_0(r_a)] +2X_3\sum_{n=1}^{\infty}\left(\frac{1-e^{-2(n-1)\theta_a}}{1-e^{-2\theta_a}}\right)J_{2n}(r_a). \tag{3.19}$$

Using the fact that $\alpha\ll1$ (equivalent to $\theta_a\ll1$), and E_1 and F_1 are more dominant than E_3 and F_3, we can obtain X_1 and X_3 with the following approximate equations:

$$X_1\simeq W_1=-\frac{1}{\gamma_1}(E_1e_1-F_1), \tag{3.20a}$$

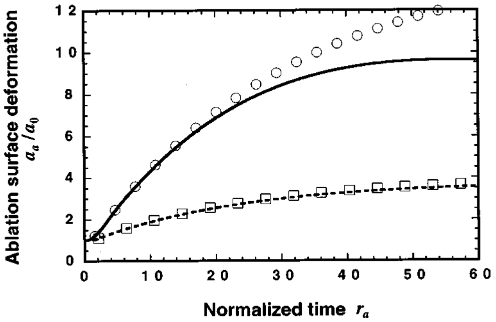

FIG. 7. Normalized amplitude of the ablation surface deformation a_a/a_0 as a function of normalized time, r_a. Dotted and solid lines show exact solutions of a_s/a_0 for absorbed laser intensities of $I=1\times10^{12}$ and 4×10^{13} W/cm^2, respectively. Squares and circles are corresponding approximate formulas.

$$X_3 \simeq W_3 \simeq -\frac{2}{\gamma_1}(E_1 e_1 - F_1). \tag{3.20b}$$

Therefore, substituting Eq. (3.20) into Eq. (3.19), and using $\theta_a \ll 1$, we can obtain

$$\frac{a_a(t)}{a_0} \simeq 1 + \frac{8M_s^2(M_s^2-1)}{(3M_s^2+1)\{2\gamma_1 M_s^2 - (\gamma_1 - 1)\}} \times \left[1 - J_0(r_a) + 4\sum_{n=1}^{\infty}\left(\frac{1-e^{-2(n-1)v_a/c_1}}{1-e^{-2v_a/c_1}}\right)J_{2n}(r_a)\right]$$

$$[r_a = kc_1 t\sqrt{1-(v_a/c_1)^2} \simeq kc_1 t], \tag{3.21}$$

where we used v_a/c_1 instead of θ_a in the exponential terms. In Ref. [9], the asymptotic value of a_a is estimated by using $v_a/c_1 \ll 1$. The results of this approximate formula and the exact solution are shown by symbols and lines in Fig. 7, respectively. The definitions of the symbols and lines are the same as those in Fig. 6. The formula agrees quite well with the exact solution for a small Mach number. The formula also agrees fairly well with the exact solution within the short duration of $r_a \lesssim 25$, even for a relatively large Mach number. The deviation of the approximate formula from the exact solution is caused by the approximation of Eq. (3.18), that is incorrect for a large Mach number. The ablation surface deformation becomes larger as the shock is stronger, as shown in Fig. 7. This can be understood as the lateral flow behind the shock front promotes more deformation of the ablation surface since the flow is larger in the stronger shock case.

Figures 8(a) and 8(b) show the laser wavelength dependence of the shock front ripple and the ablation surface deformation, respectively. They are calculated by using exact solutions. We choose $\lambda_L = 1.06$ μm (solid line), 0.53 μm (dashed line), 0.35 μm (dotted line), and 0.25 μm (dot-dashed line) as the wavelengths, called ω, 2ω, 3ω, and 4ω, respectively. The absorbed laser intensity is $I = 4\times10^{13}$ W/cm^2, and the other parameters are the same as those in Fig. 4. There is little difference among the shock front ripples, as shown in Fig. 8(a). On the contrary, the ablation surface deformation becomes smaller as the laser wavelength is shorter as shown in Fig. 8(b).

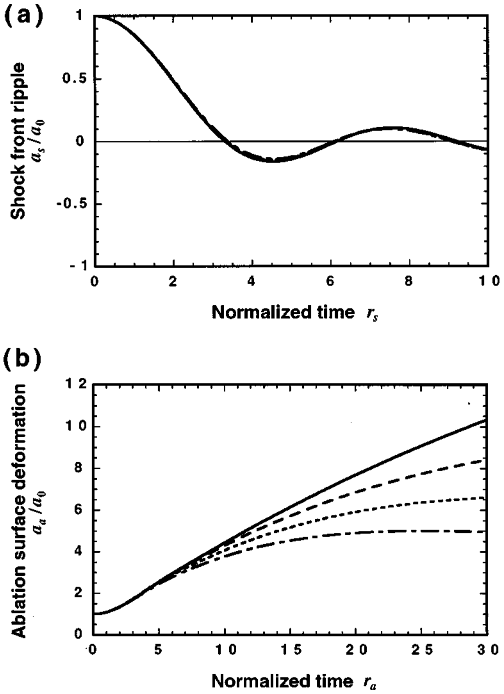

FIG. 8. (a) Normalized amplitude of the shock front ripple a_s/a_0 as a function of normalized time, r_s. Solid, dashed, dotted, and dot-dashed lines show shock front ripples for laser wavelengths of $\lambda_L = 1.06$, 0.53, 0.35, and 0.25 μm, respectively. (b) Normalized amplitude of the ablation surface deformation a_a/a_0 as a function of normalized time, r_a. The definitions of lines are the same as in (a).

This can be understood from the scaling laws of the ablation pressure and the mass ablation rate on the wavelength given by Eq. (A11). Both the pressure and the mass ablation rate become large for a short wavelength laser. However, since $p_1 \propto \lambda_L^{-2/3}$ and $\dot{m} \propto \lambda_L^{-4/3}$, the increase of the mass ablation rate dominates over that of the pressure for the short wavelength. Thus the deformation of the ablation surface is suppressed for the short wavelength laser. Since the shock is relatively strong whichever laser wavelength is used in the parameters here, we can estimate the shock front ripple and the asymptotic ablation surface deformation from Eqs. (3.16) and (3.21) as

$$\frac{a_s(r_s)}{a_0} \simeq J_0(r_s) + \frac{2}{3}J_2(r_s), \tag{3.22a}$$

$$\frac{a_{a\infty}}{a_0} \simeq 1 + \frac{4}{3\gamma_1}\left(1 + \frac{c_1}{v_a}\right), \tag{3.22b}$$

where $a_{a\infty}$ is an asymptotic value of a_a. The behavior of the shock front does not depend on the laser wavelength. On the other hand, the ablation surface deformation depends on the ablation Mach number v_a/c_1. That is, since v_a/c_1 becomes larger as λ_L becomes smaller, as shown by Eq. (A13), the ablation surface deformation becomes smaller, as shown by Eq. (3.22b). In physics, a large v_a/c_1 indicates that the ablation is promoted much more. Therefore, the ablation inhibits the deformation of the ablation surface for the short wavelength. The scaling laws of the ablation pressure and the mass ablation rate are obtained from the assumption that the

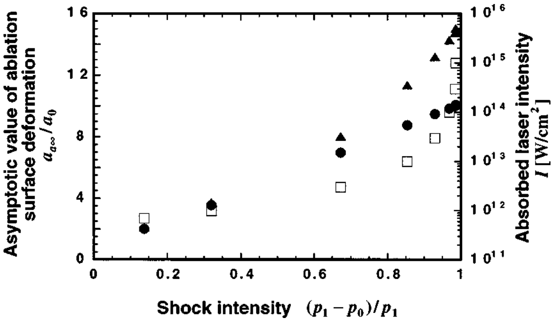

FIG. 9. Normalized asymptotic value of the ablation surface deformation $a_{a\infty}/a_0$ as a function of shock intensity, $(p_1-p_0)/p_1$. Closed circles and triangles show the exact solution and approximate formula of $a_{a\infty}/a_0$, respectively. Squares show relations between the absorbed laser intensity and shock intensity.

density of the sonic point is equal to the laser cutoff density. Thus a quantitative analysis is still required. However, the qualitative results should be correct.

Figure 9 shows the asymptotic values of a_a as a function of the shock intensity, $(p_1-p_0)/p_1$. It should be noted that in our model the shock intensity is determined by the absorbed laser intensity through the deflagration jump conditions. The relation between them is shown by squares in Fig. 9 that can provide the absorbed laser intensity dependence of the asymptotic values. We see a good agreement between the approximate formula (triangles) given by Eq. (3.21) and the exact solutions (closed circles) for the weak shock. The asymptotic value of the ablation surface deformation increases monotonously as the shock intensity increases. However, the exact solutions do not increase so much for the strong shock case, equivalent to the high absorbed laser intensity of $\gtrsim 4\times10^{13}$ W/cm^2.

One of popular quantities accessible to experimental measurement is an areal mass density. It is thus interesting to obtain information about its temporal evolution. The areal mass density ρl is given by the following equation in the laboratory system:

$$\rho l(y,t)=\int_{u_at+a_a(t)e^{iky}}^{u_st+a_s(t)e^{iky}}\{\rho_1+\delta\rho_1(x,t)e^{iky}\}dx+\int_{u_st+a_s(t)e^{iky}}^{x_t}\rho_0 dx, \tag{3.23}$$

where x_t is an initial target thickness. Noting that the initial perturbation of the areal mass density is $(\delta\rho l)_0=-\rho_0 a_0$, we can write the first-order quantity $\delta\rho l$ of Eq. (3.23) as

$$\frac{\delta\rho l(t)}{(\delta\rho l)_0}=\left(1-\frac{\rho_1}{\rho_0}\right)\frac{a_s(t)}{a_0}+\frac{\rho_1}{\rho_0}\frac{a_a(t)}{a_0}-\int_{u_at}^{u_st}\frac{\delta\rho_1(x,t)}{\rho_0 a_0}dx. \tag{3.24}$$

Substituting Eq. (3.8) through $\delta\rho_1=-\rho_1\hat{V}_1$, we obtain

$$\begin{aligned}\frac{\delta\rho l(t)}{(\delta\rho l)_0}={}&\left(1-\frac{\rho_1}{\rho_0}\right)\frac{a_s(r_s)}{a_0}+\frac{\rho_1}{\rho_0}\frac{a_a(r_a)}{a_0}-\frac{\rho_1}{\rho_0 k a_0}\\&\times\Bigg[\frac{1}{\gamma_1}\sum_{n=0}^{\infty}\{M_{2n}+N_{2n}e_{2n}\}J_{2n}(r_s)-\frac{1}{\gamma_1}\\&\times\sum_{n=0}^{\infty}\{M_{2n}e_{2n}+N_{2n}\}J_{2n}(r_a)-2\sinh\theta_s\\&\times\left(K_3+\frac{1}{\gamma_1}\right)\sum_{n=1}^{\infty}\sum_{k=0}^{n-1}\{E_{2k+1}+F_{2k+1}e_{2k+1}\}\\&\times\left\{J_{2n}(r_s)-J_{2n}\left(r_a\frac{\sinh\theta_a}{\sinh\theta_s}\right)\right\}\Bigg],\end{aligned} \tag{3.25}$$

where the coefficients M and N are

$$M_0=0,\quad M_{2n}=\sum_{k=0}^{n-1}2(-1)^{n-k-1}E_{2k+1}e^{\{2(n-k-1)+1\}\theta_s}, \tag{3.26}$$

$$N_0=0,\quad N_{2n}=\sum_{k=0}^{n-1}2(-1)^{n-k}F_{2k+1}e^{-\{2(n-k-1)+1\}\theta_a}. \tag{3.27}$$

We can thus evaluate the areal mass density perturbation by substituting Eqs. (3.6) and (3.14) into Eq. (3.25).

In Ref. [9], we compared the theoretical values with the experimental results [5]. The parameters used are the same as those in Fig. 4. Good agreement between the theory and the experiment is found in the amplitude of the shock front ripple and the areal mass density perturbation. It should be mentioned that two-dimensional simulations also predict the experimental results [5].

IV. HYDRODYNAMIC PERTURBATION DRIVEN BY NONUNIFORM LASER IRRADIATION ON A SMOOTH TARGET

A. Constant nonuniform laser irradiation

We investigate a rippled shock driven by nonuniform laser irradiation on a smooth target. In this subsection, we consider the constant nonuniformity of the laser absorption with time. Initial conditions are then given by

$$\hat{a}_s(0)=\hat{a}_a(0)=\hat{a}_0=0,\quad \hat{I}(r_a)=\hat{I}_0, \tag{4.1}$$

where $\hat{I}_0$ is a constant value. From Eq. (2.28), the latter equation in Eq. (4.1) is equivalent to

$$\phi_0=\hat{I}_0,\quad \phi_m=0\quad (m\geqslant 1). \tag{4.2}$$

In the same way as in Sec. III, we obtain an initial value of the pressure perturbation by using Eqs. (2.26) and (4.1):

$$\hat{p}_{10}=\hat{p}_1(0,\theta)=\frac{L_8}{1-L_7}\hat{I}_0\quad(\theta_a\leqslant\theta\leqslant\theta_s). \tag{4.3}$$

The separation constant must be a positive even integer to satisfy the initial conditions (4.1) and (4.3) and the boundary conditions (2.19) and (2.27). Equation (2.15) thus becomes

$$\hat{p}_1(r,\theta)=\sum_{n=0}^{\infty}\left(E_{2n}e^{-2n(\theta_s-\theta)}+F_{2n}e^{-2n(\theta-\theta_a)}\right)J_{2n}(r). \tag{4.4}$$

Using Eq. (2.13a) with Eq. (4.1), we can write a_s as

$$\hat{a}_s(r_s)=K_1(\cosh\,\theta_s)\sum_{n=0}^{\infty}(E_{2n}+F_{2n}e_{2n})\int_0^{r_s}J_{2n}(r)dr. \tag{4.5}$$

The relation obtained from Eq. (2.19) with $q=0$ is

$$\sum_{n=0}^{\infty}(E_{2n}+F_{2n}e_{2n})=0. \tag{4.6}$$

It can be seen from Eqs. (4.5) and (4.6) that $\hat{a}_s(r_s)\rightarrow 0$ when $r_s\rightarrow\infty$. Equation (4.5) can be expressed in a form

$$\hat{a}_s(r_s)=\sum_{n=0}^{\infty}G_{2n+1}J_{2n+1}(r_s), \tag{4.7}$$

with

$$G_{2n+1}=2K_1(\cosh\,\theta_s)\sum_{k=0}^{n}(E_{2k}+F_{2k}e_{2k}). \tag{4.8}$$

We can obtain the x component of the velocity perturbation by solving Eq. (2.8b) with Eq. (2.13b) in the same way as Appendix D. Then

$$\begin{aligned}\hat{v}_{x1}=&\sum_{n=0}^{\infty}\left(Q_{2n}e^{-2n(\theta_s-\theta)}+R_{2n}e^{-2n(\theta-\theta_a)}\right)J_{2n}(r)\\&+\sum_{n=0}^{\infty}S_{2n}J_{2n}\left(r\frac{\sinh\,\theta}{\sinh\,\theta_s}\right),\end{aligned} \tag{4.9}$$

where the coefficients Q, R, and S are given by

$$Q_{2n}=-\frac{1}{\gamma_1}\left(2\sum_{k=0}^{n}E_{2k}e^{2(n-k)\theta_s}-E_{2n}\right), \tag{4.10a}$$

$$R_{2n}=\frac{1}{\gamma_1}\left(2\sum_{k=0}^{n}F_{2k}e^{-2(n-k)\theta_a}-F_{2n}\right), \tag{4.10b}$$

$$S_{2n}=K_2(E_{2n}+F_{2n}e_{2n})-(Q_{2n}+R_{2n}e_{2n}). \tag{4.10c}$$

Using Eqs. (3.11), (4.4), and (4.9), the time derivative of a_a is given by

$$\frac{\dot{a}_a}{c_1}=\hat{v}_{x1}+L_9\hat{p}_1+L_{10}\hat{I}=\sum_{n=0}^{\infty}X_{2n}J_{2n}(r_a)+L_{10}\hat{I}_0 \tag{4.11}$$

where the coefficients are defined as

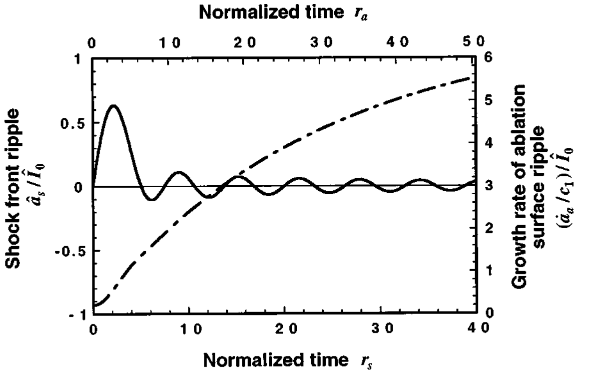

FIG. 10. Normalized amplitude of the shock front ripple $\hat{a}_s/\hat{I}_0$ as a function of normalized time, r_s; and the normalized growth rate of the ablation surface ripple $(\dot{a}_a/c_1)/\hat{I}_0$ as a function of normalized time, r_a.

$$X_0=W_0+S_0,$$

$$X_{2n}=W_{2n}+S_{2n}\alpha^{2n}+\sum_{k=0}^{n-1}(W_{2k}+S_{2k}\alpha^{2n}-X_{2k})\times\frac{(-1)^{n-k}(2n)!}{(n-k)!(n+k)!}, \tag{4.12}$$

with

$$W_{2n}=(Q_{2n}+L_9E_{2n})e_{2n}+(R_{2n}+L_9F_{2n}). \tag{4.13}$$

Integrating Eq. (4.11) with respect to r_a with the initial condition Eq. (4.1), we obtain:

$$\begin{aligned}\hat{a}_a(r_a)=&2(\cosh\,\theta_a)\sum_{n=0}^{\infty}\left[\left(\sum_{k=0}^{n}X_{2k}\right)J_{2n+1}(r_a)\right]\\&+L_{10}\hat{I}_0r_a\cosh\,\theta_a.\end{aligned} \tag{4.14}$$

In this problem, since the nonuniformity is continuously supplied by the laser, there is a finite asymptotic value of the growth rate of the ablation surface ripple, contrary to the problem in Sec. III. It is thus essential to estimate the growth rate of the ablation surface ripple given by Eq. (4.11) rather than the deformation amplitude of the ablation surface given by Eq. (4.14). Figure 10 shows the normalized shock front ripple $\hat{a}_s/\hat{I}_0$ as a function of r_s and the normalized growth rate of the ablation surface ripple $(\dot{a}_a/c_1)/\hat{I}_0$ as a function of r_a. The parameters used are the same as those in Fig. 4. Since the laser intensity perturbation drives the ablation pressure perturbation that induces the shock front ripple for an instant, the shock front ripple increase with time. On the other hand, the lateral flow behind the shock front causes the shock front ripple to decrease, as mentioned in Sec. III (see Fig. 5). Therefore, the shock front ripple increases with time at first and decays subsequently, as shown in Fig. 10. The first maximum of the dimensionless shock front ripple reaches a value of ~ 0.65 at $r_s\sim 2$ for the parameters used. The ablation surface is distorted by the lateral flow, and its growth rate increases monotonously and approaches a finite value, as shown in Fig. 10.

In the weak shock limit, it seems reasonable that the first, second, and third terms including E_0, F_0, E_2, F_2, E_4, and F_4, are dominant in the expression of a_s given by Eq. (4.7). Using the fact of $L_7 \simeq 0$ and $L_8 \simeq \frac{2}{3}$ with $L_6 \ll 1$, E_0, F_0, E_2, F_2, E_4, and F_4, are approximated from Eqs. (2.19) and (2.27), with the initial conditions Eqs. (4.1) and (4.2), as

$$E_0 \simeq \tfrac{1}{3}\hat{I}_0, \tag{4.15a}$$

$$F_0 \simeq \tfrac{1}{3}\hat{I}_0, \tag{4.15b}$$

$$E_2 \simeq -\frac{2}{3}\hat{I}_0 \frac{\gamma_1 K_5 + 2(\gamma_1 K_2 - 1)e_2}{(\gamma_1 K_2 + 1) - (\gamma_1 K_2 - 1)e_4}, \tag{4.15c}$$

$$F_2 \simeq \frac{2}{3}\hat{I}_0 \frac{\gamma_1 K_5 e_2 + 2(\gamma_1 K_2 + 1)}{(\gamma_1 K_2 + 1) - (\gamma_1 K_2 - 1)e_4}, \tag{4.15d}$$

$$E_4 \simeq \frac{-\gamma_1 K_5 (E_2 + F_2 e_2) - \frac{4}{3}\,\gamma_1 K_2 \hat{I}_0 (1 + e_4) + \frac{4}{3}\hat{I}_0 e_4}{(\gamma_1 K_2 + 1) - (\gamma_1 K_2 - 1)e_8}, \tag{4.15e}$$

$$F_4 \simeq \frac{\gamma_1 K_5 (E_2 + F_2 e_2) e_4 + \frac{4}{3}\,\gamma_1 K_2 \hat{I}_0 (1 + e_4) + \frac{4}{3}\hat{I}_0}{(\gamma_1 K_2 + 1) - (\gamma_1 K_2 - 1)e_8}, \tag{4.15f}$$

where the coefficient K_5 is

$$K_5 = 4K_1K_4 \sinh\theta_s \cosh\theta_s - 2K_2 = \frac{M_s^2 - 1}{\gamma_1 M_s^2 \beta_s}.$$

In addition, $\theta_a \ll 1$ and $e_8 \ll 1$ (equivalent to $v_a/c_1 \ll 1$), and we obtain

$$a_s(t) \simeq \frac{\delta I_0}{kI}[C_{s1}J_1(r_s) + C_{s2}J_3(r_s) + C_{s3}J_5(r_s)]$$

$$[r_s = kc_1 t\sqrt{1 - (u_s - v_{x1})^2/c_1^2}], \tag{4.16}$$

where the coefficients are given by

$$C_{s1} = \frac{\gamma_1 + 1}{3\gamma_1 \beta_s \sqrt{1 - \beta_s^2}}, \quad C_{s2} = C_{s1}\frac{(2 - \beta_s^2)M_s^2 + 3}{(2 + \beta_s^2)M_s^2 + 1},$$

$$C_{s3} = C_{s2}\frac{(2\beta_s - 1)M_s^2 + 3}{(2\beta_s + 1)M_s^2 + 1} + C_{s1}\frac{4\{2\beta_s(1 - \beta_s)^2 M_s^2 - (1 + \beta_s)^2\}}{(1 + \beta_s)^2\{(2\beta_s + 1)M_s^2 + 1\}}.$$

In Ref. [9], the shock front ripple is roughly approximated with the assumption of $C_{s3} = 0$. The results of Eq. (4.16) are shown by symbols in Fig. 11. The exact solutions are shown by lines. Squares and the dotted line and circles and the solid line represent the shock front behaviors with $I = 1 \times 10^{12}$ W/cm^2 ($M_s = 1.15$) and $I = 4 \times 10^{13}$ W/cm^2 ($M_s = 3.43$), respectively, similarly to Fig. 6. We have found that those formulas agree quite well with the exact solutions for both the small and relatively large Mach numbers. As mentioned before, the shock front ripple increases at first for both Mach numbers. However, since the lateral flow behind the shock front is larger as the shock is stronger, the shock front ripple is reversed faster (see Fig. 5). Therefore, the first peak value of the shock front ripple is smaller in the stronger shock case.

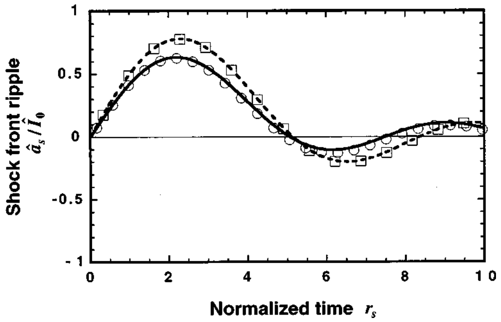

FIG. 11. Normalized amplitude of the shock front ripple $\hat{a}_s/\hat{I}_0$ as a function of normalized time, r_s. Dotted and solid lines show exact solutions of $\hat{a}_s/\hat{I}_0$ for absorbed laser intensities of $I = 1 \times 10^{12}$ and 4×10^{13} W/cm^2, respectively. Squares and circles are corresponding approximate formulas.

We take the derivative of $\dot{a}_a/c_1$ with respect to r_a in order to obtain an approximate formula for the growth rate of the ablation surface ripple in the weak shock limit:

$$\frac{d}{dr_a}\left(\frac{\dot{a}_a}{c_1}\right) = \sum_{n=0}^{\infty} Y_{2n+1}J_{2n+1}(r_a), \tag{4.17}$$

where the coefficient Y is

$$Y_1 = \tfrac{1}{2}(X_2 - 2X_0), \quad Y_{2n+1} = \tfrac{1}{2}(X_{2n+2} - X_{2n}). \tag{4.18}$$

The coefficient Y can be approximated by

$$Y_{2n+1} \simeq Y_5 e^{-2(n-2)\theta_a} \quad (n \geqslant 2). \tag{4.19}$$

Therefore, substituting Eq. (4.19) into Eq. (4.17) and integrating with respect to r_a, we obtain

$$\frac{\dot{a}_a(r_a)}{c_1} \simeq L_{10}\hat{I}_0 + X_0 + (Y_1 + Y_3)[1 - J_0(r_a)] - 2Y_3J_2(r_a) + 2Y_5\sum_{n=2}^{\infty}\left(\frac{1 - e^{-2(n-2)\theta_a}}{1 - e^{-2\theta_a}}\right)J_{2n}(r_a). \tag{4.20}$$

Using $\alpha^2 \ll 1$, we have

$$Y_1 \simeq \frac{1}{2}(W_2 - 2W_0) \simeq -\frac{1}{2\gamma_1}(E_2e_2 - F_2) - \frac{4\theta_a}{3\gamma_1}\hat{I}_0, \tag{4.21a}$$

$$Y_3 \simeq \frac{1}{2}(W_4 - W_2) \simeq -\frac{1}{2\gamma_1}(E_2e_2 - F_2) - \frac{1}{2\gamma_1}(E_4e_4 - F_4) - \frac{4\theta_a}{\gamma_1}\hat{I}_0, \tag{4.21b}$$

$$Y_5 \simeq \frac{1}{2}(W_6 - W_4) \simeq -\frac{1}{2\gamma_1}(E_4 e_4 - F_4) - \frac{1}{2\gamma_1}(E_6 e_6 - F_6) - \frac{20\theta_a}{3\gamma_1}\hat{I}_0. \tag{4.21c}$$

Since we can regard $E_4 e_4 - F_4 \simeq E_6 e_6 - F_6 \simeq -4\hat{I}_0/3$ from $e_4 \ll 1$, Eq. (4.20) becomes

$$\frac{\dot{a}_a(r_a)/c_1}{\hat{I}_0} \simeq C_{a1} + C_{a2}[1 - J_0(r_a)] - C_{a3}J_2(r_a) + C_{a4}\sum_{n=2}^{\infty}\left(\frac{1 - e^{-2(n-2)v_a/c_1}}{1 - e^{-2v_a/c_1}}\right)J_{2n}(r_a), \tag{4.22}$$

where we used v_a/c_1 instead of θ_a in the exponential terms, and the coefficients are given by

$$C_{a1} = \frac{M_s^2 + 1}{3\gamma_1 M_s^2 \beta_s},$$

$$C_{a2} = \frac{2}{3\gamma_1}\left[1 - 8\frac{v_a}{c_1} - 2\frac{(1 + 2\beta_s^2)M_s^2 + \beta_s^2}{\beta_s\{(2 + \beta_s^2)M_s^2 + 1\}}\right],$$

$$C_{a3} = \frac{4}{3\gamma_1}\left[1 - 6\frac{v_a}{c_1} - \frac{(1 + 2\beta_s^2)M_s^2 + \beta_s^2}{\beta_s\{(2 + \beta_s^2)M_s^2 + 1\}}\right],$$

$$C_{a4} = \frac{8}{3\gamma_1}\left[1 - 5\frac{v_a}{c_1}\right].$$

In Ref. [9], the asymptotic value of $\dot{a}_a$ is estimated by using $v_a/c_1 \ll 1$. Integrating Eq. (4.22) with respect to r_a with the initial condition Eq. (4.1), we obtain the amplitude of the ablation surface deformation as

$$a_a(t) \simeq \frac{\delta I_0}{kI}\Bigg[(C_{a1} + C_{a2})r_a - 2C_{a2}J_1(r_a) - 2(C_{a2} + C_{a3}) \times J_3(r_a) - 2\sum_{n=2}^{\infty}\left\{C_{a2} + C_{a3} - \frac{C_{a4}}{1 - e^{-2v_a/c_1}} \times\left(n - 1 - \frac{1 - e^{-2(n-1)v_a/c_1}}{1 - e^{-2v_a/c_1}}\right)\right\}J_{2n+1}(r_a)\Bigg]$$

$$[r_a = kc_1 t\sqrt{1 - (v_a/c_1)^2} \simeq kc_1 t]. \tag{4.23}$$

Figure 12 shows the approximate formula (symbols) and the exact solution (lines) of the growth rate of the ablation surface ripple. The definitions of symbols and lines are the same as those in Fig. 11. We have good agreement between both results not only in the weak shock case but also in the relatively strong shock case, contrary to the relation between the approximate formula and the exact solution of the ablation surface deformation in Fig. 7. The growth rate of the ablation surface ripple is larger in the stronger shock case because of the larger lateral flow behind the shock front.

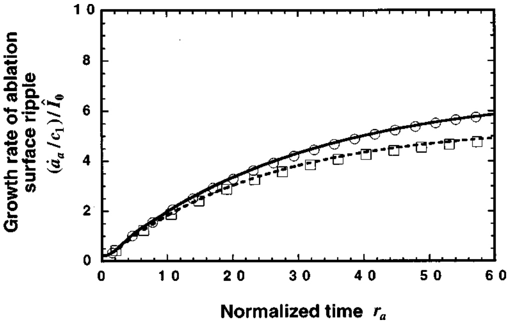

FIG. 12. Normalized growth rate of the ablation surface ripple $(\dot{a}_a/c_1)/\hat{I}_0$ as a function of normalized time, r_a. Dotted and solid lines show exact solutions of $(\dot{a}_a/c_1)/\hat{I}_0$ for absorbed laser intensities of $I = 1\times10^{12}$ and 4×10^{13} W/cm^2, respectively. Squares and circles are corresponding approximate formulas.

Figures 13(a) and 13(b) show the laser wavelength dependence of the shock front ripple and the growth rate of the ablation surface ripple, respectively. Solid, dashed, dotted, and dot-dashed lines are the results of $\lambda_L = 1.06$, 0.53, 0.35, and 0.25 μm, respectively. Similarly to Fig. 8, there is little differences in the shock front ripples among the different laser wavelengths. However, the growth rate of the ablation surface ripple becomes smaller as the laser wavelength becomes shorter. Since the shock is relatively strong in the parameters used here, the behaviors of the shock front ripple become the same as shown in Eq. (4.16). On the other hand, since v_a/c_1 is larger the shorter

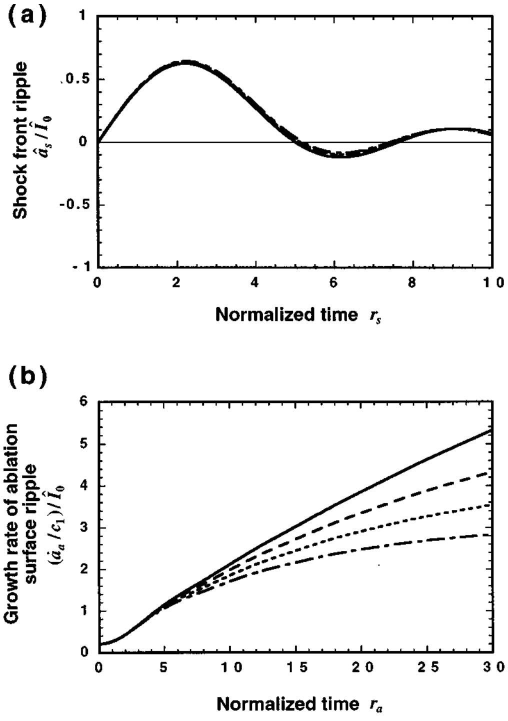

FIG. 13. (a) Normalized amplitude of the shock front ripple $\hat{a}_s/\hat{I}_0$ as a function of normalized time, r_s. Solid, dashed, dotted, and dot-dashed lines show shock front ripples for laser wavelengths of $\lambda_L = 1.06$, 0.53, 0.35, and 0.25 μm, respectively. (b) Normalized growth rate of the ablation surface ripple $(\dot{a}_a/c_1)/\hat{I}_0$ as a function of normalized time, r_a. The definitions of lines are the same as in (a).

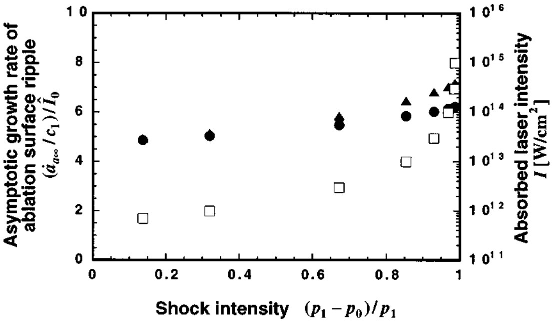

FIG. 14. Normalized asymptotic growth rate of the ablation surface ripple $(\dot{a}_{a\infty}/c_1)/\hat{I}_0$ as a function of shock intensity, $(p_1-p_0)/p_1$. Closed circles and triangles show exact solutions and approximate formulas of $(\dot{a}_{a\infty}/c_1)/\hat{I}_0$, respectively. Squares show relations between the absorbed laser intensity and shock intensity.

λ_L is, as mentioned in Sec. III, the growth rate of the ablation surface ripple becomes smaller for the short wavelength, as shown by Eq. (4.22). These features are the same as those in the case of the initial target roughness discussed in Sec. III.

Figure 14 shows the normalized asymptotic values of $\dot{a}_a$ as a function of the shock intensity, $(p_1-p_0)/p_1$. We have a good agreement between the approximate values (triangles) given by Eq. (4.22) and the exact solutions (closed circles) for the weak shock. The asymptotic value increases monotonously as the shock intensity increases; however, the increase is small compared with the asymptotic value of a_a in Fig. 9. That is, $(\dot{a}_{a\infty}/c_1)/\hat{I}_0$ is 5–7 for low to high shock intensity $[0<(p_1-p_0)/p_1<1]$. This is mainly due to the normalization of $\dot{a}_a$, i.e., $\dot{a}_a$ is normalized by the sound speed c_1 that increases as the shock intensity increases. Squares can provide the absorbed laser intensity dependence of the asymptotic value.

We have used the CJ deflagration jump condition at the ablation surface, which leads to the intensity dependence of the ablation pressure being given approximately by $p_1(I)\propto I^{2/3}$, as shown in Appendix A. This dependence gives a good approximation when the direct deposition of the laser energy is near the critical density. However, when the energy deposition is distributed over some distance from the critical density, a different intensity dependence of the ablation pressure should be used. Various models give different dependences; for example, Ref. [27] summarizes that $p_1\propto I^{\zeta}$, $0.57\lesssim\zeta\lesssim0.86$ for different models. Since our theory is based on linear theory, both the amplitude of the shock front ripple and the growth rate of the ablation surface deformation are approximately proportional to ζ. The results shown in Figs. 10–13 are obtained for the case $\zeta=\frac{2}{3}$. The results change accordingly for different dependences of the ablation pressure.

B. Nonuniform laser irradiation oscillating with time

We also consider a case when the nonuniformity of the absorbed laser intensity oscillates with time,

$$\hat{I}=\hat{I}_0\cos(\omega t), \tag{4.24}$$

where $\hat{I}_0$ and ω are the amplitude and the oscillation frequency of the nonuniformity, respectively. Since variables at the ablation surface become functions of the normalized time r_a, as mentioned above we rewrite $\hat{I}$ as a function of r_a:

$$\hat{I}=\hat{I}_0\cos(\hat{\omega}r_a), \tag{4.25}$$

where the normalized oscillation frequency $\hat{\omega}$ is defined by

$$\hat{\omega}=\frac{\omega}{kc_1}\cosh\,\theta_a. \tag{4.26}$$

Using Eq. (2.28), the coefficient ϕ becomes

$$\phi_{2n}=\frac{(-1)^n}{(2n)!}\hat{\omega}^{2n},\quad \phi_{2n+1}=0. \tag{4.27}$$

Initial conditions of the shock front ripple and the ablation surface deformation are

$$\hat{a}_s(0)=\hat{a}_a(0)=\hat{a}_0=0. \tag{4.28}$$

The initial value of the pressure perturbation $\hat{p}_{10}$ is given by Eq. (4.3). Since the separation constant in $\hat{p}_1$ must be a positive even integer to satisfy the initial and boundary conditions, $\hat{p}_1$ is given by Eq. (4.4). We can thus determine the coefficients E and F by solving Eqs. (2.19) and (2.27) with Eqs. (4.3) and (4.27), and also determine all other coefficients. Using those results, the shock front ripple is expressed by Eq. (4.5) or (4.7).

In the weak shock limit, it seems reasonable that the first, second, and third terms including E_0, F_0, E_2, F_2, E_4, and F_4, are dominant in Eq. (4.7) within $\hat{\omega}\lesssim1$. These coefficients are approximated from Eqs. (2.19) and (2.27) with Eqs. (4.3) and (4.27) as

$$E_0\simeq\frac{1}{3}\hat{I}_0, \tag{4.29a}$$

$$F_0\simeq\frac{1}{3}\hat{I}_0, \tag{4.29b}$$

$$E_2\simeq-\frac{2}{3}\hat{I}_0\frac{\gamma_1K_5+2(\gamma_1K_2-1)e_2}{(\gamma_1K_2+1)-(\gamma_1K_2-1)(1-2\hat{\omega}^2)e_4}, \tag{4.29c}$$

$$F_2\simeq\frac{2}{3}\hat{I}_0\frac{\gamma_1K_5e_2+2(\gamma_1K_2+1)(1-2\hat{\omega}^2)}{(\gamma_1K_2+1)-(\gamma_1K_2-1)e_4}, \tag{4.29d}$$

$$E_4 \simeq \frac{-\gamma_1 K_5(E_2+F_2 e_2) - \frac{4}{3}\gamma_1 K_2 \hat{I}_0 - \frac{4}{3}\hat{I}_0 e_4(\gamma_1 K_2 - 1)(1-8\hat{\omega}^2+8\hat{\omega}^4)}{(\gamma_1 K_2+1)-(\gamma_1 K_2-1)e_8}, \tag{4.29e}$$

$$F_4 \simeq \frac{\gamma_1 K_5(E_2+F_2 e_2)e_4 + \frac{4}{3}\gamma_1 K_2 \hat{I}_0 e_4 + \frac{4}{3}\hat{I}_0(\gamma_1 K_2 + 1)(1-8\hat{\omega}^2+8\hat{\omega}^4)}{(\gamma_1 K_2+1)-(\gamma_1 K_2-1)e_8}, \tag{4.29f}$$

where we used $L_7 \simeq 0$ and $L_8 \simeq \frac{2}{3}$. Substituting these coefficients into Eq. (4.7) and using $\theta_a \ll 1$ and $e_8 \ll 1$ (equivalent to $v_a/c_1 \ll 1$), we obtain the approximate formula of the shock front ripple within $\hat{\omega} \lesssim 1$:

$$a_s(t) \simeq \frac{\delta I_0}{kI}[C_{s1}J_1(r_s)+C_{s2}J_3(r_s)+C_{s3}J_5(r_s)] \quad [r_s = kc_1 t\sqrt{1-(u_s-v_{x1})^2/c_1^2}], \tag{4.30}$$

with

$$C_{s1} = \frac{\gamma_1+1}{3\gamma_1\beta_s\sqrt{1-\beta_s^2}}, \quad C_{s2} = C_{s1}\frac{(2-\beta_s^2)M_s^2+3-4\hat{\omega}^2 M_s^2(1-\beta_s^2)}{(2+\beta_s^2)M_s^2+1},$$

$$C_{s3} = C_{s2}\frac{(2\beta_s-1)M_s^2+3}{(2\beta_s+1)M_s^2+1} - C_{s1}\frac{4(1+\beta_s)^2-8M_s^2\beta_s(1-\beta_s)^2(1-8\hat{\omega}^2+8\hat{\omega}^4)}{(1+\beta_s)^2\{(2\beta_s+1)M_s^2+1\}}.$$

Figure 15 shows the oscillation frequency dependence of the normalized shock front ripple $\hat{a}_s/\hat{I}_0$ as a function of r_s. Symbols and lines show the results of the approximate formulas and the exact solutions, respectively. Circles and the solid line and squares and the dotted line represent the results for the oscillation frequencies $\hat{\omega}=1$ and 2, respectively. The absorbed laser intensity is $I=1\times10^{12}$ W/cm^2, the laser wavelength is $\lambda_L=0.53$ μm, and the other parameters used are the same as those in Fig. 4. Using Eq. (4.26) in those parameters, the oscillation period of the perturbed laser intensity, T_{os}, is written as

$$T_{\mathrm{os}} = \frac{2\pi\cosh\theta_a}{\hat{\omega}kc_1} = \frac{2\pi}{\hat{\omega}kc_1\sqrt{1-(v_a/c_1)^2}}$$

$$\simeq 0.063\frac{[\lambda\ (\mu\mathrm{m})]}{\hat{\omega}}\ \mathrm{ns}. \tag{4.31}$$

Therefore, if the nonuniform wavelength is $\lambda=100$ μm, $\hat{\omega}=1$ means that the laser nonuniformity oscillates in the period with $T_{\mathrm{os}}=6.3$ ns. As shown in Fig. 15, the approximate formulas agree well with the exact solutions in spite of $\hat{\omega}\gtrsim1$ because of the relatively weak laser intensity. The first maximum value of the shock front ripple becomes smaller, and its oscillation period becomes shorter as the oscillation frequency becomes higher. This can be understood as the oscillating nonuniform laser irradiation reverses the ablation pressure perturbation that distorts the shock front ripple for an instant. The decay of the shock front ripple becomes slower for the higher oscillation frequency because the shock front ripple is affected by the constrained oscillation of perturbations at the ablation surface induced by the perturbed laser intensity. However, the shock front ripple no longer depends on the frequency in the weak shock limit, since the information of the ablation surface cannot reach the shock front, as mentioned in Sec. III. That is clear from the fact that Eq. (4.30) becomes Eq. (4.16) in that limit ($M_s \simeq \beta_s \simeq 1$).

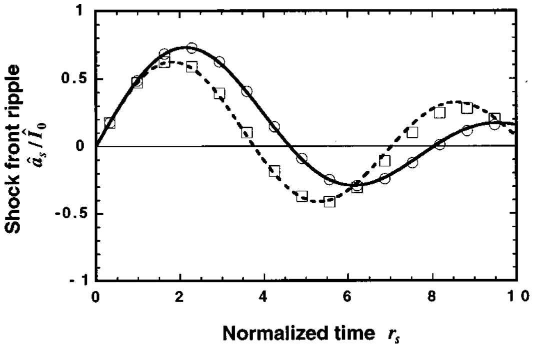

FIG. 15. Normalized amplitude of the shock front ripple $\hat{a}_s/\hat{I}_0$ as a function of normalized time, r_s. Solid and dotted lines show exact solutions of $\hat{a}_s/\hat{I}_0$ for normalized oscillation frequencies $\hat{\omega}=1$ and 2, respectively. Circles and squares are corresponding approximate formulas of $\hat{a}_s/\hat{I}_0$.

Let us consider the behavior of the ablation surface deformation. The growth rate and the amplitude of the ablation surface ripple are given by

$$\frac{\dot{\hat{a}}_a}{c_1} = \sum_{n=0}^{\infty} X_{2n}J_{2n}(\hat{\omega}r_a) + L_{10}\hat{I}_0\cos(\hat{\omega}r_a), \tag{4.32}$$

$$\hat{a}_a(r_a) = 2(\cosh\theta_a)\sum_{n=0}^{\infty}\left[\left(\sum_{k=0}^{n}X_{2k}\right)J_{2n+1}(\hat{\omega}r_a)\right] + L_{10}\hat{I}_0\cosh\theta_a\frac{\sin(\hat{\omega}r_a)}{\hat{\omega}}, \tag{4.33}$$

where the coefficients X are

$$X_0 = W_0 + S_0,$$

$$X_{2n} = \frac{1}{\hat{\omega}^{2n}}\left[W_{2n} + S_{2n}\alpha^{2n} + \sum_{k=0}^{n-1} (W_{2k} + S_{2k}\alpha^{2n} - X_{2k}\hat{\omega}^{2n}) \times \frac{(-1)^{n-k}(2n)!}{(n-k)!(n+k)!} \right], \tag{4.34}$$

with W and S given by Eqs. (4.13) and (4.10c), respectively.

In the weak shock limit, we can obtain the approximate formula for the growth rate of the ablation surface ripple as follows. It is not necessary to take the derivative of $\dot{a}_a/c_1$ with respect to r_a, contrary to Sec. IV A, because it seems reasonable that within $\hat{\omega} \gtrsim 1$ the coefficients X are given by

$$X_{2(2k+1)} \simeq X_2 \quad (k \geqslant 0), \quad X_{2(2k)} \simeq X_4 \quad (k \geqslant 1). \tag{4.35}$$

Therefore, substituting Eq. (4.35) into Eq. (4.32) and using a familiar formula $J_0(r_a) + 2\Sigma_{n=1}^{\infty} J_{2n}(r_a) = 1$, we obtain the approximate formula

$$\frac{\dot{a}_a(r_a)}{c_1} \simeq \frac{1}{4}(X_2 + X_4) + \left(X_0 - \frac{1}{2}X_4 \right) J_0(\hat{\omega} r_a) + \left[\frac{1}{4}(X_4 - X_2) + L_{10}\hat{I}_0 \right] \cos(\hat{\omega} r_a). \tag{4.36}$$

X_0, X_2, and X_4 are given by using Eqs. (4.10), (4.13), and (4.34):

$$X_0 = W_0 + S_0 \simeq \frac{2}{3}\hat{I}_0(K_2 + L_9), \tag{4.37a}$$

$$X_2 \simeq \frac{W_2 - 2W_0}{\hat{\omega}^2} + 2(W_0 + S_0) \simeq -\frac{1}{\gamma_1\hat{\omega}^2}(E_2e_2 - F_2) + \frac{4}{3}\hat{I}_0(K_2 - L_9) - \frac{8\theta_a}{3\gamma_1\hat{\omega}^2}\hat{I}_0, \tag{4.37b}$$

$$X_4 \simeq \frac{W_4 - 2W_2 + 6W_0}{\hat{\omega}^4} + 4\frac{W_2 - 2W_0}{\hat{\omega}^2} + 2(W_0 + S_0) \simeq \frac{1}{\gamma_1}\left(\frac{2}{\hat{\omega}^4} - \frac{4}{\hat{\omega}^2} \right)(E_2e_2 - F_2) - \frac{1}{\gamma_1\hat{\omega}^4}(E_4e_4 - F_4) + \frac{4}{3}\hat{I}_0(K_2 + L_9), \tag{4.37c}$$

where we used $\alpha^2 \ll 1$. Since we can regard $E_4e_4 - F_4 \simeq -4\hat{I}_0(1 - 8\hat{\omega}^2 + 8\hat{\omega}^4)/3$ from $e_4 \ll 1$, Eq. (4.36) becomes

$$\frac{\dot{a}_a(r_a)/c_1}{\hat{I}_0} \simeq C_{a1} + C_{a2}J_0(\hat{\omega} r_a) + C_{a3}\cos(\hat{\omega} r_a), \tag{4.38}$$

where the coefficients are given by

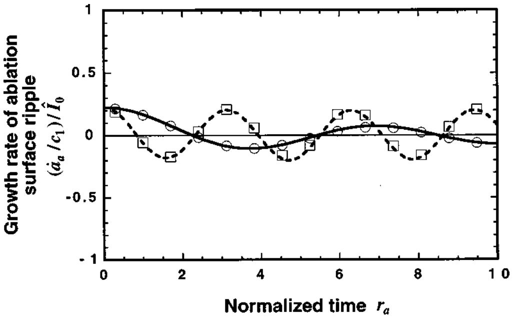

FIG. 16. Normalized growth rate of the ablation surface ripple $(\dot{a}_a/c_1)/\hat{I}_0$ as a function of normalized time, r_a. Solid and dotted lines show exact solutions of $(\dot{a}_a/c_1)/\hat{I}_0$, for normalized oscillation frequencies $\hat{\omega} = 1$ and 2, respectively. Circles and squares are corresponding approximate formulas of $(\dot{a}_a/c_1)/\hat{I}_0$.

$$C_{a1} = \frac{1}{3\gamma_1}\left[\frac{M_s^2 + 1}{M_s^2\beta_s} - \left(\frac{2}{\hat{\omega}^4} - \frac{5}{\hat{\omega}^2} \right) d_1 + \frac{d_2}{\hat{\omega}^4} \right],$$

$$C_{a2} = \frac{2}{3\gamma_1}\left[\left(\frac{2}{\hat{\omega}^4} - \frac{4}{\hat{\omega}^2} \right) d_1 - \frac{d_2}{\hat{\omega}^4} \right],$$

$$C_{a3} = \frac{1}{3\gamma_1}\left[-\left(\frac{2}{\hat{\omega}^4} - \frac{3}{\hat{\omega}^2} \right) d_1 + \frac{d_2}{\hat{\omega}^4} \right],$$

with

$$d_1 = \frac{\{(2\beta_s^2 + 1)M_s^2 + \beta_s^2\} - \hat{\omega}^2\{(M_s^2 + 1)(1 + \beta_s^2) + 4M_s^2\beta_s^2\}}{\beta_s\{(2 + \beta_s^2)M_s^2 + 1\}},$$

$$d_2 = 1 - 8\hat{\omega}^2 + 8\hat{\omega}^4.$$

Integrating Eq. (4.38) with respect to r_a with the initial condition Eq. (4.28), we obtain the amplitude of the ablation surface deformation as

$$a_a(t) \simeq \frac{\delta I_0}{kI}\left[C_{a1}r_a + C_{a2}\int_0^{r_a} J_0(\hat{\omega} r)dr + \frac{C_{a3}}{\hat{\omega}}\sin(\hat{\omega} r_a) \right] \left(r_a \simeq kc_1 t, \quad \hat{\omega} \simeq \frac{\omega}{kc_1} \right). \tag{4.39}$$

Figure 16 shows the oscillation frequency dependence of the normalized growth rate of the ablation surface ripple $(\dot{a}_a/c_1)/\hat{I}_0$ as a function of r_a. The results of the approximate formulas and the exact solutions are shown by symbols and lines. The definitions of symbols and lines are the same as those in Fig. 15. The parameters used are also the same. The approximate formulas agree quite well with the exact solutions. The growth rate of the ablation surface ripple oscillates with the same period as the laser nonuniformity, because the growth is directly induced by the pressure perturbation at the ablation surface. We show the constant term C_{a1} in Eq. (4.38) that corresponds to the averaged growth

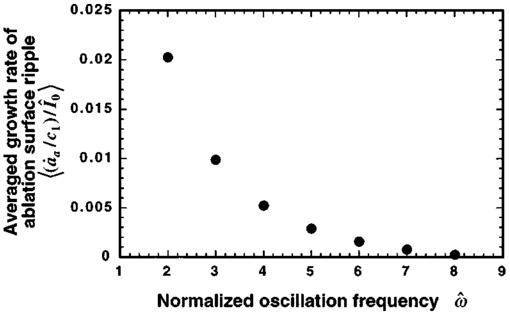

FIG. 17. Time averaged growth rate of the ablation surface ripple $\langle(\dot{a}_a/c_1)/\hat{I}_0\rangle$ as a function of normalized oscillation frequency, $\hat{\omega}$.

rate of the ablation surface ripple $\langle(\dot{a}_a/c_1)/\hat{I}_0\rangle$, as a function of $\hat{\omega}$ in Fig. 17. That value decays as $\hat{\omega}$ increases, as shown by Eq. (4.38). Since the higher oscillation frequency smoothes the nonuniform ablation pressure much more, the averaged growth rate of the ablation surface ripple decreases. It is not easy to obtain the exact solution for a high frequency limit because the convergence of the summation in Eq. (4.32). Therefore, the approximate formula may not be accurate in the high frequency limit. However, it is important to estimate the growth rate in order to understand qualitatively the behavior of the ablation surface deformation. In the high frequency limit, there is no averaged growth rate of the ablation surface ripple for a weak shock, but a finite averaged growth rate may exist for a relatively strong shock, as shown by Eq. (4.38), since a fluid motion driven by laser irradiation for an instant remains. Appendix E shows the exact solution and approximate formula in the case that laser nonuniformity is given by $\hat{I}=\hat{I}_0\sin(\omega t)$ instead of Eq. (4.24).

V. CONCLUSIONS

We have developed an analytical model for linear growth of hydrodynamic perturbations induced by nonuniform laser ablation due to initial surface roughness of a target or nonuniform laser irradiation. It is shown that a shock front ripple and deformation of an ablation surface driven by the nonuniform laser ablation interact with each other through a sound wave and an entropy wave in the shock compressed region. We have explicitly shown analytic solutions expressing the shock front ripple and the ablation surface deformation by solving a linear wave equation with the RH jump condition at the shock front, the CJ deflagration jump condition at the ablation surface, and plausible boundary conditions at the sonic point.

An amplitude of the shock front ripple oscillates and decays with time. The asymptotic oscillation period is $(kc_1)^{-1}$, and the decay rate is proportional to the reciprocal of the square root of time, $t^{-1/2}$. The amplitude of the ripple decays rapidly compared with that driven by a rippled rigid piston, because of mass ablation. In the case of nonuniform laser irradiation, the first maximum of the ripple amplitude depends weakly on the shock intensity; for example, the normalized amplitude $ka_s/(\delta I_0/I)$ is ~ 0.65 for a laser intensity of 4×10^{13} W/cm^2.

In the case of target surface roughness, deformation of the ablation surface increases slowly compared with the oscillation period of the shock front ripple, and approaches a finite value. The growth of the deformation is thus different from the RM instability. On the other hand, in the case of constant nonuniform laser irradiation the growth rate of the ablation surface approaches a finite value. We obtain scaling laws for the asymptotic amplitude and growth rate with respect to laser intensity and laser wavelength. In both cases, it is shown that laser irradiation with high intensity (up to $\sim 4\times10^{13}$ W/cm^2) causes the ablation surface to distort, while laser irradiation with short wavelength inhibits its deformation because of the mass ablation effect.

The behaviors of the shock front ripple and the ablation surface deformation are also investigated in the case when the nonuniformity of the laser irradiation oscillates with time. It is shown that the deformation of the ablation surface is inhibited for a high frequency of $\omega/(kc_1)\gg 1$. We obtain approximate formulas for temporal behaviors of the shock front ripple and the ablation surface deformation in the weak shock limit. Those formulas agree with the exact solutions not only for a weak shock but also for a relatively strong shock.

ACKNOWLEDGMENTS

We are grateful to Dr. J. G. Wouchuk for valuable suggestions relating the asymptotic formulas. We thank Dr. M. Murakami, Dr. Y. Shimuta, M. Honda, N. Matsui, K. Shigemori, Dr. M. Nakai, Professor H. Azechi, Professor N. Miyanaga, and Professor K. Mima for many useful discussions. We acknowledge support from the Japan Society for the Promotion of Science (JSPS).

APPENDIX A: CHAPMAN-JOUGUET DEFLAGRATION JUMP CONDITIONS

We can write the mass, momentum, and energy conservation equations across the ablation layer (between regions 1 and 2) as

$$\rho_1\overline{v_1}=\rho_2\overline{v_2}=\dot{m}, \tag{A1a}$$

$$p_1+\rho_1\overline{v_1^2}=p_2+\rho_2\overline{v_2^2}, \tag{A1b}$$

$$h_1+\frac{1}{2}\overline{v_1^2}+\frac{I}{\rho_1\overline{v_1}}=h_2+\frac{1}{2}\overline{v_2^2}, \tag{A1c}$$

where $\overline{v_1}=u_a-v_{x1}$ (flow velocity across the ablation surface); $\overline{v_2}=u_a-v_{x2}$ (flow velocity across the sonic point); I is the absorbed laser energy; $\dot{m}$ is the mass ablation rate; and h is the enthalpy, $h=\gamma p/[(\gamma-1)\rho]$. Eliminating $\overline{v_2}$ from Eqs. (A1a) and (A1b), we obtain

$$\overline{v_1^2}=\frac{p_1-p_2}{\rho_1-\rho_2}\frac{\rho_2}{\rho_1}. \tag{A2}$$

By using V instead of ρ, this is expressed as

$$\frac{\overline{v_1}}{V_1}=\sqrt{\frac{p_1-p_2}{V_2-V_1}}. \tag{A3}$$

In the same way, we obtain

$$\frac{\overline{v}_2}{V_2}=\sqrt{\frac{p_1-p_2}{V_2-V_1}}. \tag{A4}$$

Substituting Eqs. (A3) and (A4) into Eq. (A1c), the energy conservation equation becomes

$$\frac{\gamma_1}{\gamma_1-1}p_1V_1+\frac{1}{2}V_1^2\frac{p_1-p_2}{V_2-V_1}+\frac{I}{\dot{m}}$$

$$=\frac{\gamma_2}{\gamma_2-1}p_2V_2+\frac{1}{2}V_2^2\frac{p_1-p_2}{V_2-V_1}. \tag{A5}$$

Then

$$\left(\frac{\gamma_1+1}{\gamma_1-1}V_1-V_2\right)p_1-\left(\frac{\gamma_2+1}{\gamma_2-1}V_2-V_1\right)p_2=-\frac{2I}{\dot{m}}. \tag{A6}$$

On the other hand, by using Eqs. (A1a) and (A3), $\dot{m}$ is written as

$$\dot{m}=\rho_1\overline{v}_1=\frac{\overline{v}_1}{V_1}=\sqrt{\frac{p_1-p_2}{V_2-V_1}}. \tag{A7}$$

If there is no energy absorption, namely, $I=0$, Eq. (A6) corresponds to the Hugoniot curve in the p-V diagram.

We briefly discuss the absorbed laser intensity (I) dependence and the laser wavelength (λ_L) dependence of the ablation pressure (p_1), the mass ablation rate ($\dot{m}$), and the ablation Mach number (v_a/c_1) [19]. Using Eq. (2.7) and the fact of $V_2\gg V_1$ in general, the relation of the pressures at the ablation surface 1 and at the sonic point 2 is approximately given by

$$p_2/p_1\simeq\tfrac{1}{2}. \tag{A8}$$

The mass ablation rate thus becomes

$$\dot{m}=\sqrt{\frac{p_1-p_2}{V_2-V_1}}\simeq\sqrt{\frac{p_1}{2V_2}}. \tag{A9}$$

Substituting Eqs. (A8) and (A9) into Eq. (A6), and eliminating p_2 and V_1, we can write p_1 as

$$p_1\simeq\left[\frac{32I^2}{(2+\nu_2)^2V_2}\right]^{1/3}, \tag{A10}$$

where $\nu_2=(\gamma_2+1)/(\gamma_2-1)$. In addition, using $V_2\propto\lambda_L^2$, we obtain equations expressing I and λ_L dependences of the ablation pressure p_1 and the mass ablation rate $\dot{m}$ as

$$p_1\propto\left(\frac{I}{\lambda_L}\right)^{2/3},\quad \dot{m}\propto\left(\frac{I}{\lambda_L^4}\right)^{1/3}. \tag{A11}$$

The ablation pressure is thus larger as the laser intensity is larger and the laser wavelength is shorter. The ablation Mach number is estimated in the following way. By using the mass conservation across the ablation layer [see Eq. (2.5)], and the fact that the fluid velocity at the sonic point relative to the ablation surface is equal to the isothermal sound speed [see Eq. (2.7)], we obtain $\rho_1v_a=\rho_2c_2$. Then

$$\frac{v_a}{c_1}=\frac{\rho_2c_2}{\rho_1c_1}=\sqrt{\frac{p_2\rho_2}{\gamma_1p_1\rho_1}}. \tag{A12}$$

In addition, using $p_2/p_1\simeq\frac{1}{2}$ and $\rho_2\propto1/\lambda_L^2$, and using $\rho_1\simeq$ const in the case of a strong shock wave, we obtain

$$\frac{v_a}{c_1}\propto\frac{1}{\lambda_L}. \tag{A13}$$

That is, the ablation Mach number v_a/c_1 becomes larger as λ_L becomes smaller. It should be noted that $v_a/c_1\ll1$ from the assumption of $V_2\gg V_1$.

APPENDIX B: LINEARIZED CHAPMAN-JOUGUET DEFLAGRATION JUMP CONDITIONS

Linearized equations of Eqs. (A1a)–(A1c) are given by [30]

$$\delta\rho_1\overline{v}_1+\rho_1\delta\overline{v}_1=\delta\rho_2\overline{v}_2+\rho_2\delta\overline{v}_2, \tag{B1a}$$

$$\delta p_1+\delta\rho_1\overline{v}_1^2+2\rho_1\overline{v}_1\delta\overline{v}_1=\delta p_2+\delta\rho_2\overline{v}_2^2+2\rho_2\overline{v}_2\delta\overline{v}_2, \tag{B1b}$$

$$\frac{\gamma_1}{\gamma_1-1}\left(\frac{\delta p_1}{\rho_1}-\frac{p_1}{\rho_1^2}\delta\rho_1\right)+\overline{v}_1\delta\overline{v}_1+\frac{\delta I}{\rho_1\overline{v}_1}-\frac{I}{(\rho_1\overline{v}_1)^2}\delta(\rho_1\overline{v}_1)$$

$$=\frac{\gamma_2}{\gamma_2-1}\left(\frac{\delta p_2}{\rho_2}-\frac{p_2}{\rho_2^2}\delta\rho_2\right)+\overline{v}_2\delta\overline{v}_2. \tag{B1c}$$

Eliminating $\delta\overline{v}_2$ from Eqs. (B1a) and (B1b), we obtain

$$2\rho_1(\overline{v}_1-\overline{v}_2)\delta\overline{v}_1=\delta p_1-\delta p_2+\delta\rho_1(2\overline{v}_1\overline{v}_2-\overline{v}_1^2)-\delta\rho_2\overline{v}_2^2. \tag{B2}$$

Using $\overline{v}_1/\overline{v}_2=\rho_2/\rho_1$ given by Eq. (A1a), $\delta\overline{v}_1$ becomes

$$\frac{\delta\overline{v}_1}{\overline{v}_1}=\frac{\delta p_1-\delta p_2}{2(p_1-p_2)}-\frac{2\rho_1-\rho_2}{2\rho_1(\rho_1-\rho_2)}\delta\rho_1+\frac{\rho_1}{2\rho_2(\rho_1-\rho_2)}\delta\rho_2. \tag{B3}$$

Using V instead of ρ and using $\delta\overline{v}_1=\delta u_a-\delta v_{x1}=\dot{a}_a-\delta v_{x1}$, Eq. (B3) is

$$\frac{\delta\overline{v}_1}{\overline{v}_1}=\frac{\dot{a}_a-\delta v_{x1}}{u_a-v_{x1}}=\frac{\delta p_1-\delta p_2}{2(p_1-p_2)}+\frac{2V_2-V_1}{2(V_2-V_1)}\frac{\delta V_1}{V_1}$$

$$-\frac{\delta V_2}{2(V_2-V_1)}. \tag{B4}$$

In the same way, $\delta\overline{v}_2$ is given by

$$\frac{\delta\overline{v_2}}{\overline{v_2}}=\frac{\dot{a}_a-\delta v_{x2}}{u_a-v_{x2}}=\frac{\delta p_1-\delta p_2}{2(p_1-p_2)}-\frac{\delta V_1}{2(V_1-V_2)}+\frac{2V_1-V_2}{2(V_1-V_2)}\frac{\delta V_2}{V_2}. \tag{B5}$$

On the other hand, Eq. (B1c) is written by using V instead of ρ as

$$\frac{\gamma_1}{\gamma_1-1}(\delta p_1 V_1+p_1\delta V_1)+\overline{v_1}^2\frac{\delta\overline{v_1}}{\overline{v_1}}+\frac{\delta I}{I}\frac{I}{\dot{m}}-\frac{I}{\dot{m}}\frac{\delta\dot{m}}{\dot{m}}=\frac{\gamma_2}{\gamma_2-1}(\delta p_2 V_2+p_2\delta V_2)+\overline{v_2}^2\frac{\delta\overline{v_2}}{\overline{v_2}}, \tag{B6}$$

where $\delta\dot{m}$ is given by linearizing Eq. (A7):

$$\frac{\delta\dot{m}}{\dot{m}}=\frac{\delta p_1-\delta p_2}{2(p_1-p_2)}-\frac{\delta V_2-\delta V_1}{2(V_2-V_1)}. \tag{B7}$$

Substituting Eqs. (B4), (B5), and (B7) into Eq. (B6), we obtain

$$L_1\frac{\delta p_1}{p_1}+L_2\frac{\delta V_1}{V_1}+L_3\frac{\delta p_2}{p_1}+L_4\frac{\delta V_2}{V_1}=L_5\frac{\delta I}{I}. \tag{B8}$$

The coefficients are

$$L_1=\left(1-\nu_2\frac{V_2}{V_1}\right)\frac{p_2}{p_1}+\frac{I}{\dot{m}}\frac{3p_1-2p_2}{p_1-p_2}, \tag{B9a}$$

$$L_2=-\left(1+\nu_2\frac{p_2}{p_1}\right)\frac{V_2}{V_1}+\frac{I}{\dot{m}}\frac{2V_2-V_1}{V_2-V_1}, \tag{B9b}$$

$$L_3=-\left(1-\nu_2\frac{V_2}{V_1}\right)-\frac{I}{\dot{m}}\frac{p_1}{p_1-p_2}, \tag{B9c}$$

$$L_4=\left(1+\nu_2\frac{p_2}{p_1}\right)-\frac{I}{\dot{m}}\frac{V_1}{V_2-V_1}, \tag{B9d}$$

$$L_5=\frac{2I}{\dot{m}}, \tag{B9e}$$

where $\nu=(\gamma+1)/(\gamma-1)$. Equations (B4), (B5), and (B8) correspond to the linearized equations (A3), (A4), and (A6), respectively.

Next, let us show that the coefficients in Eqs. (B4), (B5), and (B8) are expressed by only a new variable $\overline{M}=\gamma_1(v_a/c_1)^2$, where v_a is the ablation velocity $v_a=\overline{v_1}$. By using the mass conservation between the ablation surface and the sonic point [Eq. (A1a)], and using the fact that the fluid velocity at the sonic point relative to the ablation surface is equal to the isothermal sound speed, we obtain $\rho_1\overline{v_1}=\rho_2\overline{v_2}=\rho_2 c_2$. Then

$$\overline{M}=\gamma_1\left(\frac{\overline{v_1}}{c_1}\right)^2=\gamma_1\left(\frac{\rho_2 c_2}{\rho_1 c_1}\right)^2=\frac{p_2 V_1}{p_1 V_2}. \tag{B10}$$

On the other hand, using $\overline{v_2}=c_2=\sqrt{p_2 V_2}$ and Eq. (A4), another relation is obtained:

$$\overline{v_2}=\sqrt{p_2 V_2}=V_2\sqrt{\frac{p_1-p_2}{V_2-V_1}}. \tag{B11}$$

Then

$$\frac{V_1}{V_2}=2-\frac{p_1}{p_2}. \tag{B12}$$

Therefore, using Eqs. (B10) and (B12), the following relations are shown:

$$\frac{p_2}{p_1}=\frac{1+\overline{M}}{2}, \tag{B13a}$$

$$\frac{V_2}{V_1}=\frac{1+\overline{M}}{2\overline{M}}. \tag{B13b}$$

We can consider $p_2/p_1\simeq\frac{1}{2}$ and $\overline{M}\ll 1$ because of $V_2\gg V_1$ in general.

Substituting Eq. (B13) into Eqs. (B4) and (B5), we can write

$$\frac{\dot{a}_a-\delta v_{x1}}{v_a}=\frac{\hat{p}_1-\hat{p}_2+\hat{V}_1-\overline{M}\hat{V}_2}{1-\overline{M}} \tag{B14a}$$

$$\frac{\dot{a}_a-\delta v_{x2}}{c_2}=\frac{1}{1-\overline{M}}\left(\hat{p}_1-\hat{p}_2+\overline{M}\hat{V}_1+\frac{\overline{M}(1-3\overline{M})}{1+\overline{M}}\hat{V}_2\right). \tag{B14b}$$

In the same way, the coefficients of Eq. (B8), $L_1\sim L_6$, are written as

$$L_1=\frac{1+\overline{M}}{\overline{M}}-\nu_1\frac{2-\overline{M}}{1-\overline{M}}+\nu_2\frac{(1+\overline{M})^2}{4\overline{M}(1-\overline{M})}, \tag{B15a}$$

$$L_2=-\nu_1\frac{1}{1-\overline{M}}+\nu_2\frac{(1+\overline{M})^2}{4(1-\overline{M})}, \tag{B15b}$$

$$L_3=-\frac{1+3\overline{M}}{2\overline{M}}+\nu_1\frac{1}{1-\overline{M}}+\nu_2\frac{(1+\overline{M})(1-3\overline{M})}{4\overline{M}(1-\overline{M})}, \tag{B15c}$$

$$L_4=\frac{1-\overline{M}}{2}+\nu_1\frac{\overline{M}}{1-\overline{M}}+\nu_2\frac{(1+\overline{M})(1-3\overline{M})}{4(1-\overline{M})}, \tag{B15d}$$

$$L_5=\frac{1-\overline{M}^2}{2\overline{M}}-\nu_1+\nu_2\frac{(1+\overline{M})^2}{4\overline{M}}. \tag{B15e}$$

APPENDIX C: BOUNDARY CONDITIONS AT THE SHOCK FRONT, ABLATION SURFACE, AND SONIC POINT

The boundary conditions introduced in Sec. II C are obtained by linearizing the RH jump condition at the shock front and the CJ jump condition at the ablation surface. Therefore, the hydrodynamic motion at the boundaries is re-

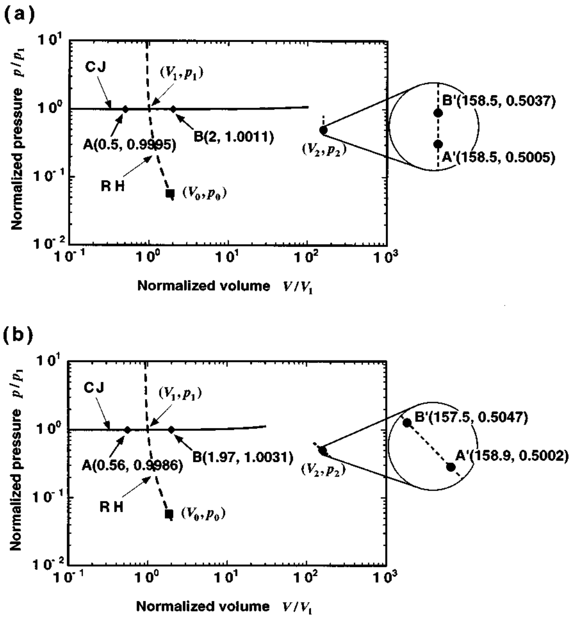

FIG. 18. Normalized p-V diagrams for shock and laser ablation. Squares show the uniform state ahead of shock. The dashed line shows the RH curve passing through the uniform state. Dotted lines show states at the sonic point when (a) $\delta V_2 = 0$ and (b) $\delta T_2 = 0$. Solid lines are states at the ablation surface corresponding to the states (dotted lines) at the sonic point. Closed circles show the states at the sonic point corresponding to rhombuses on the solid lines.

stricted to satisfy the jump conditions. Since no perturbation exists ahead of the shock, the perturbed variables at the shock front change along the RH curve [dashed line in Figs. 18(a) and 18(b)], more rigorously along the tangent of the RH curve at the point (p_1, V_1) because of the linearization. The parameters used in Figs. 18(a) and 18(b) are a laser intensity of $I = 4\times 10^{13}$ W/cm^2, a laser wavelength of $\lambda_L = 0.53$ μm, a mass density of $\rho_0 = 1.06$ g/cm^3 (CH target), a pressure of $p_0 = 0.703$ Mbar (equivalent to $T_0 = 1$ eV), and isentropic exponents of $\gamma_0 = 3$, $\gamma_1 = 3$, and $\gamma_2 = \frac{5}{3}$. In Fig. 18, the square shows a uniform state ahead of the shock, and the RH curve (dashed line) passes through the uniform state.

On the other hand, the perturbation at the ablation surface propagates out through the ablation layer, although the perturbation in the isothermal expansion region does not affect the surface beyond the sonic point. Thus we have to allow the perturbations at the sonic point. The linearized CJ deflagration jump conditions of Eqs. (2.20) and (2.21) give the relations between the perturbations at the ablation surface and those at the sonic point. However, they are not enough to give a unique relation among the variables at the ablation surface and the sonic point. The additional condition of $\delta V_2 = 0$ or $\delta T_2 = 0$ results in the unique relations which are shown by solid lines $(\delta p_1, \delta V_1)$ at the ablation surface and by dotted lines $(\delta p_2, \delta V_2)$ at the sonic point in Figs. 18(a) and 18(b) for the cases of $\delta V_2 = 0$ and $\delta T_2 = 0$, respectively. For example, in the case of $\delta V_2 = 0$, the perturbation of the ablation pressure and the specific volume at the ablation surface change along the solid line in Fig. 18(a); equivalently, when the pressure and specific volume perturbations at the ablation surface change along the solid line, the pressure perturbation at the sonic point changes along the dotted line $(\delta V_2 = 0)$. In Fig. 18(a), the perturbed states at the ablation surface given by the rhombuses on the solid line, $(V_1 + \delta V_1, p_1 + \delta p_1) = (0.5, 0.9995)$ and $(2, 1.0011)$, correspond to the perturbed states at the sonic point given by the closed circles on the dotted line, $(V_2, p_2 + \delta p_2) = (158.5, 0.5005)$ and $(158.5, 0.5037)$, respectively. Figure 18(b) shows the same as Fig. 18(a) for the case of $\delta T_2 = 0$. As clearly seen from Figs. 18(a) and 18(b), the relations of the pressure and density perturbations at the ablation surface are almost the same in both cases of $\delta V_2 = 0$ and $\delta T_2 = 0$. The perturbation of the ablation pressure is very small compared with that of the specific volume at the ablation surface. Even if a large perturbation of the specific volume at the ablation surface is present, it results in a small pressure change at the sonic point.

APPENDIX D: DERIVATION OF THE LOCAL VELOCITY PERTURBATION IN THE SHOCK COMPRESSED REGION

In the case of target surface roughness, we show how to solve the partial differential equation (2.8b) with the boundary condition (2.13b), where $\hat{p}_1$ is given by Eq. (3.3). Using normalized quantities, Eq. (2.8b) is written as

$$\frac{\partial \hat{v}_{x1}}{\partial \hat{t}} = -\frac{1}{\gamma_1}\frac{\partial \hat{p}_1}{\partial \hat{x}}. \tag{D1}$$

By using Eq. (2.11), the following derivation is obtained:

$$\begin{aligned}\frac{\partial \hat{p}_1}{\partial \hat{x}} &= -(\sinh\theta)\frac{\partial \hat{p}_1}{\partial r} + \frac{1}{r}(\cosh\theta)\frac{\partial \hat{p}_1}{\partial \theta} = -\frac{1}{2}(\sinh\theta)\sum_{n=0}^{\infty}\left(E_{2n+1}e^{-(2n+1)(\theta_s-\theta)} + F_{2n+1}e^{-(2n+1)(\theta-\theta_a)}\right)(J_{2n}(r)\\ &\quad - J_{2n+2}(r)) + \frac{1}{2}(\cosh\theta)\sum_{n=0}^{\infty}\left(E_{2n+1}e^{-(2n+1)(\theta_s-\theta)} - F_{2n+1}e^{-(2n+1)(\theta-\theta_a)}\right)(J_{2n}(r) + J_{2n+2}(r))\\ &= \frac{1}{2}(E_1 e^{-\theta_s} - F_1 e^{\theta_a})J_0(r) + \frac{1}{2}\sum_{n=1}^{\infty}(E_{2n+1}e^{-\theta_s} + E_{2n-1}e^{\theta_s})e^{-2n(\theta_s-\theta)}J_{2n}(r)\\ &\quad - \frac{1}{2}\sum_{n=1}^{\infty}(F_{2n+1}e^{\theta_a} + F_{2n-1}e^{-\theta_a})e^{-2n(\theta-\theta_a)}J_{2n}(r).\end{aligned} \tag{D2}$$

On the other hand, $\partial\hat{v}_{x1}/\partial\hat{t}$ is written through the relation with Eq. (2.11) as

$$\frac{\partial\hat{v}_{x1}}{\partial\hat{t}}=(\cosh\,\theta)\frac{\partial\hat{v}_{x1}}{\partial r}-\frac{1}{r}(\sinh\,\theta)\frac{\partial\hat{v}_{x1}}{\partial\theta}. \tag{D3}$$

$\hat{v}_{x1}$ should be expressed by the following equation in order for Eqs. (D2) and (D3) to satisfy Eq. (D1):

$$\hat{v}_{x1}=\sum_{n=0}^{\infty}\,(Q_{2n+1}e^{-(2n+1)(\theta_s-\theta)}+R_{2n+1}e^{-(2n+1)(\theta-\theta_a)})J_{2n+1}(r), \tag{D4}$$

where the coefficients Q and R are determined by the coefficients E and F, as mentioned below. Since the general solution of $\hat{v}_{x1}$ is obtained by adding an integral constant to Eq. (D4), we can write

$$\hat{v}_{x1}=\sum_{n=0}^{\infty}\,(Q_{2n+1}e^{-(2n+1)(\theta_s-\theta)}+R_{2n+1}e^{-(2n+1)(\theta-\theta_a)})J_{2n+1}(r)+f(\hat{x}), \tag{D5}$$

where $\hat{x}=r\,\sinh\,\theta$ is noted. Substituting Eq. (D5) into Eq. (D3), we obtain

$$\begin{aligned}\frac{\partial\hat{v}_{x1}}{\partial\hat{t}}=a\frac{1}{2}(Q_1e^{-\theta_s}+R_1e^{\theta_a})J_0(r)+\frac{1}{2}\sum_{n=1}^{\infty}\,&(Q_{2n+1}e^{-\theta_s}\\ &-Q_{2n-1}e^{\theta_s})e^{-2n(\theta_s-\theta)}J_{2n}(r)+\frac{1}{2}\sum_{n=1}^{\infty}\,(R_{2n+1}e^{\theta_a}\\ &-R_{2n-1}e^{-\theta_a})e^{-2n(\theta-\theta_a)}J_{2n}(r).\end{aligned} \tag{D6}$$

Therefore, after substituting Eqs. (D2) and (D6) into Eq. (D1), and setting the coefficients of $e^{-2n(\theta_s-\theta)}J_{2n}(r)$ and $e^{-2n(\theta-\theta_a)}J_{2n}(r)$ equal to zero for all n, Q, and R are given by the equations

$$Q_{2n+1}=-\frac{1}{\gamma_1}\left(2\sum_{k=0}^{n}\,E_{2k+1}e^{2(n-k)\theta_s}-E_{2n+1}\right), \tag{D7a}$$

$$R_{2n+1}=\frac{1}{\gamma_1}\left(2\sum_{k=0}^{n}\,F_{2k+1}e^{-2(n-k)\theta_a}-F_{2n+1}\right). \tag{D7b}$$

Let us determine the integral constant f. Since Eq. (2.13b) gives the relation between $\hat{v}_{x1}$ and $\hat{p}_1$ at the shock front ($r=r_s$ and $\theta=\theta_s$), we obtain

$$\begin{aligned}v_{x1}(r_s,\theta_s)&=\sum_{n=0}^{\infty}\,(Q_{2n+1}+R_{2n+1}e^{-(2n+1)(\theta_s-\theta_a)})J_{2n+1}(r_s)\\ &\quad+f(r_s\,\sinh\,\theta_s)\\ &=K_2\sum_{n=0}^{\infty}\,(E_{2n+1}+F_{2n+1}e^{-(2n+1)(\theta_s-\theta_a)}).\end{aligned} \tag{D8}$$

Noting $\hat{x}=r_s\,\sinh\,\theta_s=r\sinh\,\theta$, f is written as

$$f(r\,\sinh\,\theta)=\sum_{n=0}^{\infty}\,S_{2n+1}J_{2n+1}\left(r\frac{\sinh\,\theta}{\sinh\,\theta_s}\right), \tag{D9}$$

with

$$\begin{aligned}S_{2n+1}=&K_2(E_{2n+1}+F_{2n+1}e^{-(2n+1)(\theta_s-\theta_a)})\\ &-(Q_{2n+1}+R_{2n+1}e^{-(2n+1)(\theta_s-\theta_a)}).\end{aligned} \tag{D10}$$

Therefore, $\hat{v}_{x1}$ is given by

$$\begin{aligned}\hat{v}_{x1}=&\sum_{n=0}^{\infty}\,(Q_{2n+1}e^{-(2n+1)(\theta_s-\theta)}\\ &+R_{2n+1}e^{-(2n+1)(\theta-\theta_a)})J_{2n+1}(r)\\ &+\sum_{n=0}^{\infty}\,S_{2n+1}J_{2n+1}\left(r\frac{\sinh\,\theta}{\sinh\,\theta_s}\right).\end{aligned} \tag{D11}$$

In the same way, the y component of the velocity perturbation is obtained by solving Eq. (2.8c) with Eq. (2.13d):

$$\begin{aligned}\hat{v}_{y1}=&\sum_{n=0}^{\infty}\,(T_{2n}e^{-2n(\theta_s-\theta)}+U_{2n}e^{-2n(\theta-\theta_a)})J_{2n}(r)\\ &+\sum_{n=0}^{\infty}\,V_{2n}J_{2n}\left(r\frac{\sinh\,\theta}{\sinh\,\theta_s}\right),\end{aligned} \tag{D12}$$

where the coefficients are

$$T_0=0,\quad T_{2n}=\frac{2}{\gamma_1}\sum_{k=0}^{n-1}\,E_{2k+1}e^{\{2(n-k)-1\}\theta_s}, \tag{D13a}$$

$$U_0=0,\quad U_{2n}=\frac{2}{\gamma_1}\sum_{k=0}^{n-1}\,F_{2k+1}e^{-\{2(n-k)-1\}\theta_a}, \tag{D13b}$$

$$V_{2n}=K_4G_{2n}-(T_{2n}+U_{2n}e_{2n}). \tag{D13c}$$

Next we show $\hat{v}_{x1}$ and $\hat{v}_{y1}$ in the case of laser nonuniform irradiation described in Sec. IV A. By solving Eq. (2.8b) with Eq. (2.13b) where $\hat{p}_1$ is given by Eq. (4.4), $\hat{v}_{x1}$ is written as

$$\begin{aligned}\hat{v}_{x1}=&\sum_{n=0}^{\infty}\,(Q_{2n}e^{-2n(\theta_s-\theta)}+R_{2n}e^{-2n(\theta-\theta_a)})J_{2n}(r)\\ &+\sum_{n=0}^{\infty}\,S_{2n}J_{2n}\left(r\frac{\sinh\,\theta}{\sinh\,\theta_s}\right),\end{aligned} \tag{D14}$$

where the coefficients Q, R, and S are given by

$$Q_{2n}=-\frac{1}{\gamma_1}\left(2\sum_{k=0}^{n}\,E_{2k}e^{2(n-k)\theta_s}-E_{2n}\right), \tag{D15a}$$

$$R_{2n}=\frac{1}{\gamma_1}\left(2\sum_{k=0}^{n}\,F_{2k}e^{-2(n-k)\theta_a}-F_{2n}\right), \tag{D15b}$$

$$S_{2n}=K_2(E_{2n}+F_{2n}e_{2n})-(Q_{2n}+R_{2n}e_{2n}), \tag{D15c}$$

and by solving Eq. (2.8c) with Eq. (2.13d), $\hat{v}_{y1}$ is written as

$$\begin{aligned}\hat{v}_{y1}=&\sum_{n=0}^{\infty}(T_{2n+1}e^{-(2n+1)(\theta_s-\theta)}\\&+U_{2n+1}e^{-(2n+1)(\theta-\theta_a)})J_{2n+1}(r)\\&+\sum_{n=0}^{\infty}V_{2n+1}J_{2n+1}\left(r\frac{\sinh\theta}{\sinh\theta_s}\right),\end{aligned} \tag{D16}$$

where the coefficients are

$$T_{2n+1}=\frac{2}{\gamma_1}\sum_{k=0}^{n}E_{2k}e^{\{2(n-k)+1\}\theta_s}, \tag{D17a}$$

$$U_{2n+1}=\frac{2}{\gamma_1}\sum_{k=0}^{n}F_{2k}e^{-\{2(n-k)+1\}\theta_a}, \tag{D17b}$$

$$V_{2n+1}=K_4G_{2n+1}-(T_{2n+1}+U_{2n+1}e_{2n+1}). \tag{D17c}$$

APPENDIX E: A CASE WHERE LASER NONUNIFORMITY IS GIVEN BY A SINE FUNCTION

We mention a case where the nonuniformity of the absorbed laser intensity is given by

$$\hat{I}=\hat{I}_0\sin(\hat{\omega}r_a). \tag{E1}$$

The coefficients ϕ become

$$\phi_{2n}=0, \quad \phi_{2n+1}=\frac{(-1)^n}{(2n+1)!}\hat{\omega}^{2n+1}. \tag{E2}$$

Therefore, the coefficients E_m and F_m with odd m solved from Eqs. (2.19) and (2.27) dominate perturbed variables. The pressure perturbation is thus expressed by Eq. (3.3). The shock front ripple is given by Eq. (3.6), and the growth rate of the ablation surface ripple is given by

$$\frac{\dot{a}_a}{c_1}=\sum_{n=0}^{\infty}X_{2n+1}J_{2n+1}(\hat{\omega}r_a)+L_{10}\hat{I}_0\sin(\hat{\omega}r_a), \tag{E3}$$

where the coefficients X are

$$X_1=\frac{1}{\hat{\omega}}(W_1+S_1\alpha),$$

$$X_{2n+1}=\frac{1}{\hat{\omega}^{2n+1}}\left[W_{2n+1}+S_{2n+1}\alpha^{2n+1}+\sum_{k=0}^{n-1}(W_{2k+1}+S_{2k+1}\alpha^{2n+1}-X_{2k+1}\hat{\omega}^{2n+1})\frac{(-1)^{n-k}(2n+1)!}{(n-k)!(n+k+1)!}\right], \tag{E4}$$

with W and S given by Eqs. (3.13) and (3.10c), respectively.

In the weak shock limit, it seems reasonable that a_s is written within $\hat{\omega}\lesssim 1$ as

$$a_s(t)\simeq\frac{\delta I_0}{kI}[C_{s1}J_2(r_s)+C_{s2}J_4(r_s)+C_{s3}J_6(r_s)] \quad [r_s=kc_1t\sqrt{1-(u_s-v_{x1})^2/c_1^2}], \tag{E5}$$

where the coefficients are

$$C_{s1}=\frac{4(\gamma_1+1)M_s^2\hat{\omega}}{3\gamma_1\beta_s(3M_s^2+1)}, \quad C_{s2}=C_{s1}\frac{2M_s^2(1+3\beta_s^2)-(M_s^2-3)(3+\beta_s^2)+(3-4\hat{\omega}^2)(1-\beta_s^2)(3M_s^2+1)}{2M_s^2(1+3\beta_s^2)+(M_s^2+1)(3+\beta_s^2)},$$

$$C_{s3}=C_{s2}\frac{(2\beta_s-1)M_s^2+3}{(2\beta_s+1)M_s^2+1}-C_{s1}\frac{4(1+\beta_s)^3-2\beta_s(3M_s^2+1)(1-\beta_s)^2(5-20\hat{\omega}^2+16\hat{\omega}^4)}{(1+\beta_s)^3\{(2\beta_s+1)M_s^2+1\}}.$$

In that limit, it seems reasonable that the growth rate of the ablation surface ripple is obtained by

$$\frac{\dot{a}_a(r_a)/c_1}{\hat{I}_0}\simeq C_{a1}\int_0^{\hat{\omega}r_a}J_0(r)dr+C_{a2}\sin(\hat{\omega}r_a), \tag{E6}$$

where the coefficients are

$$C_{a1}=\frac{1}{3\gamma_1}\left[-\left(\frac{1}{\hat{\omega}^2}-4\right)d_1+\frac{1}{\hat{\omega}^2}d_2\right], \quad C_{a2}=\frac{1}{3\gamma_1}\left[\left(\frac{1}{\hat{\omega}^2}-2\right)d_1-\frac{1}{\hat{\omega}^2}d_2\right],$$

with

$$d_1=\frac{(1+2\beta_s^2)M_s^2+1}{\beta_s(3M_s^2+1)},\quad d_2=\frac{4M_s^2(M_s^2-1)(1-\beta_s^2)^2+(3-4\hat{\omega}^2)(3M_s^2+1)\{2M_s^2\beta_s^2(3+\beta_s^2)+(M_s^2+1)(1+3\beta_s^2)\}}{\beta_s(3M_s^2+1)\{2M_s^2(1+3\beta_s^2)+(M_s^2+1)(3+\beta_s^2)\}}.$$

Integrating Eq. (E6) with respect to r_a with the initial condition Eq. (4.28), we obtain the amplitude of the ablation surface deformation as

$$a_a(t)\simeq\frac{\delta I_0}{kI}\left[C_{a1}\int_0^{r_a}dr\int_0^{\hat{\omega}r}dr'J_0(r')+\frac{C_{a2}}{\hat{\omega}}\{1-\cos(\hat{\omega}r_a)\}\right]\quad\left(r_a\simeq kc_1t,\quad\hat{\omega}\simeq\frac{\omega}{kc_1}\right).\tag{E7}$$

These results are the same as those in the case when the laser nonuniformity is given by Eq. (4.25). That is, the first maximum value of the shock front ripple becomes smaller, and its oscillation period becomes shorter as the oscillation frequency becomes higher. The decay of the shock front ripple becomes slower. On the other hand, the growth rate of the ablation surface ripple oscillates in the same period as the laser nonuniformity. Its averaged value decays as the oscillation frequency increases.

[1] J. Nuckolls *et al.*, Nature (London) **239**, 139 (1972).

[2] H. Takabe and T. Ishii, Jpn. J. Appl. Phys. 32, 5675 1993).

[3] S. Chandrasekhar, *Hydrodynamic and Hydromagnetic Stability* (Oxford University Press, London, 1968), Chap. 10.

[4] I. Hachisu *et al.*, Astrophys. J. **390**, 230 (1992).

[5] T. Endo *et al.*, Phys. Rev. Lett. **74**, 3608 (1995); Phys. Rev. Lett. **75**, 2908(E) (1995).

[6] H. Takabe *et al.*, Phys. Fluids **28**, 3676 (1985).

[7] J. Grun *et al.*, Phys. Rev. Lett. **58**, 2672 (1987).

[8] B. Remington *et al.*, Phys. Rev. Lett. **67**, 3259 (1991).

[9] R. Ishizaki and K. Nishihara, Phys. Rev. Lett. **78**, 1920 (1997).

[10] R. J. Taylor *et al.*, Phys. Rev. Lett. **76**, 1643 (1996).

[11] D. H. Kalantar *et al.*, Phys. Rev. Lett. **76**, 3574 (1996).

[12] M. Desselberger *et al.*, Phys. Rev. Lett. **74**, 2961 (1995).

[13] M. Dunne *et al.*, Phys. Rev. Lett. **75**, 3858 (1995).

[14] H. Azechi *et al.*, Phys. Plasmas **4**, 4079 (1997).

[15] P. M. Zaidel, J. Appl. Math. Mech. **24**, 316 (1960).

[16] M. G. Briscoe and A. A. Kovitz, J. Fluid Mech. **31**, 529 (1968).

[17] R. D. Richtmyer, Commun. Pure Appl. Math. **13**, 297 (1960).

[18] R. Ishizaki *et al.*, Phys. Rev. E **53**, 5592 (1996).

[19] H. Takabe *et al.*, J. Phys. Soc. Jpn. **45**, 2001 (1978).

[20] J. G. Wouchuk and K. Nishihara, Phys. Plasmas **3**, 3761 (1996).

[21] J. G. Wouchuk and K. Nishihara, Phys. Plasmas **4**, 1028 (1997).

[22] S. G. Glendinning *et al.*, Phys. Rev. E **54**, 4473 (1996).

[23] J. Lindl, Phys. Plasmas **2**, 3933 (1995).

[24] H. Nakano *et al.*, J. Appl. Phys. **73**, 2122 (1993).

[25] N. Miyanaga *et al.*, *Plasma Physics and Controlled Nuclear Fusion Research 1994* (IAEA, Vienna, 1996), Vol. 3, pp. 153–158.

[26] W. M. Manheimer and D. G. Colombant, Phys. Fluids **27**, 983 (1984).

[27] M. H. Key, in *Physics of Laser Plasma*, edited by A. Rubenchik and S. Witkowski (North-Holland, Amsterdam, 1991), Vol. 3, Chap. 14.

[28] W. M. Manheimer *et al.*, Phys. Fluids **25**, 1644 (1982).

[29] Y. Shimuta and K. Nishihara (private communication).

[30] J. G. Wouchuk and A. R. Piriz, Phys. Plasmas **2**, 493 (1995).